Design & control of a novel thermal haptic device

Uijttewaal, A.H.

Award date:
2022

EINDHOVEN UNIVERSITY OF TECHNOLOGY

DEPARTMENT OF MECHANICAL ENGINEERING
ENERGY TECHNOLOGY & DYNAMICS AND CONTROL GROUP

Design & control of a novel thermal haptic device

Phase 2, Graduation project

"This report was made in accordance with the TU/e Code of Scientific Conduct for the Master thesis"

Author:
A.H. Uijttewaal, 1018183

Coordinators:
Dr. Ir. M.F.M. Speetjens
Dr. Ir. I.A. Kuling

Eindhoven, April 5, 2022

Contents

1 Introduction

Virtual reality is nowadays a technology that every dedicated consumer can access for a reasonable price [2]. A simulated environment is displayed to the user with a headset containing audio and visual instruments together with two hand consoles that provide position feedback to the computer. Since humans are visually oriented this experience is already quite satisfactory. However, significant progress can be made in emulating thermal feedback. It has been shown that thermal sensation is crucial in distinguishing between objects with varying thermal properties [13], by providing thermal feedback to the user a more realistic experience can be achieved. A practical example is the difference felt comparing a steel object to a wooden one. When both objects are room temperature the steel object will appear to be colder, this results from its higher heat conductivity. More heat is transported away from your hand creating a colder sensation.

Current research on haptic systems for hands can be divided into the following main categories: providing force feedback, texture feedback and thermal feedback. These technologies combined give the user an optimal virtual experience. The technology of force feedback has progressed up to a point that several systems are commercially available on the private market [24]. These systems consist of some sort of glove that houses actuators and sensors that track the position of the fingers and apply the desired force feedback in order to emulate the feeling of holding a solid object. The technology of texture and thermal feedback has progressed but is still considered to be in its infancy [15],[31]. This means further research has to be performed in order to develop the necessary technology. In the future these texture and thermal feedback systems could be mounted on a force feedback glove to create a complete virtual experience.

In order to provide a realistic experience both hot and cold sensations have to be emulated. Research has showed that human skin has 3.5 times more cold receptors compared to hot receptors [30] . This in combination with the fact the room temperature is lower that our skin temperature means that cooling should be a crucial aspect of any thermal haptic device. Because of the relative difficulty of cooling many concepts in the past have only focused on creating a heating device [16] [18][23]. There are only a few experimental setups that have provided both a form of heating and cooling. And even fewer devices have been compact enough to wear. Projects that have made a first attempt have relied on Peltier elements [10][20][17][12], or liquid cooling using water [19]. A obstacle is that heat cannot be eliminated, as dictated by the first law of thermodynamics. This means that in order to cool part of the hand the heat has to be transported away including additional heat created by the cooling system.

Both mentioned cooling systems have drawbacks, commercial Peltier elements are only 5-10% efficient and therefore even in optimal conditions drastically increase the heat load of the cooling system [1]. In parallel this creates a high power load on the system. The Peltier elements work on low voltage direct current, this together with the low efficiency creates the need for a large amount of direct current. The electronic hardware needed to create this direct current is extensive and be difficult to convert in a wearable system. A drawback of a liquid setup is that it has many moving components compared to zero moving components of the Peltier element setup. This creates more complexity and the extra components can make the setup bulky. The added complexity creates a challenge from a control perspective, since more processes can influence the output of the system. The Peltier element is generally more easily to control over a small temperature range. However, when cooling output is desired for a longer time the heat generation can make the system uncontrollable. Before the Peltier element is written off it is useful to gain some insight into the working principle of a thermoelectric cooler which is the subject of the following section.

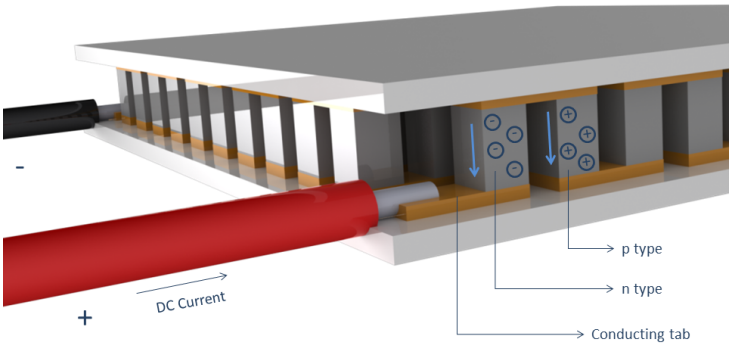

Figure 1.1: Peltier module, pn-junctions in series

Peltier elements are a type of thermoelectric device consisting of two semi-conducting materials. The contact between the materials creates a pn-junction. When a voltage difference is applied the electrons will move across the junction from a high energy state into a low energy state. This low energy state corresponds to a lower temperature creating a cold side, and the other side being hot. When the current is reversed the effect also reverses, the cold side is now hot and vice versa. This way a Peltier element can transport heat in both directions. The effect in a single junction is small, in order to compensate this many pn-junctions are formed in series, as seen in figure 1.1. For this element to work efficiently the materials must have low thermal conductivity and high electrical conductivity. This is a drawback since these properties are related to each other. Materials with high electrical conductivity will almost always have high thermal conductivity. This is a consequence of the underlying physics, more free electrons in a material will increase both thermal conductivity and electrical conductivity. A dimensionless parameter commonly used to characterise the performance of a thermoelectric element is the figure of Merit (Zt) shown in equation 1.1.

$$Zt = \frac{\sigma S^2 T}{\kappa} \tag{1.1}$$

Variable	Description	Unit
S	Seebeck Coefficient	V/K
σ	electical conductivity	S/m
T	temperature	K
κ	thermal conductivity	W $m^{-1}K^{-1}$

Table 1.1: Variables

In order to be useful the figure of merit has to be higher than 1, and favorably much higher to increase efficiency. The most popular commercially available combination of materials is Bismuth Telluride which can achieve a Zt of 1.3 [11]. This option will however still have limited efficiency. Advances in material sciences and applied physics may create better thermoelectric coolers but as of the start of this project no breakthroughs in this field are expected to occur in the near future.

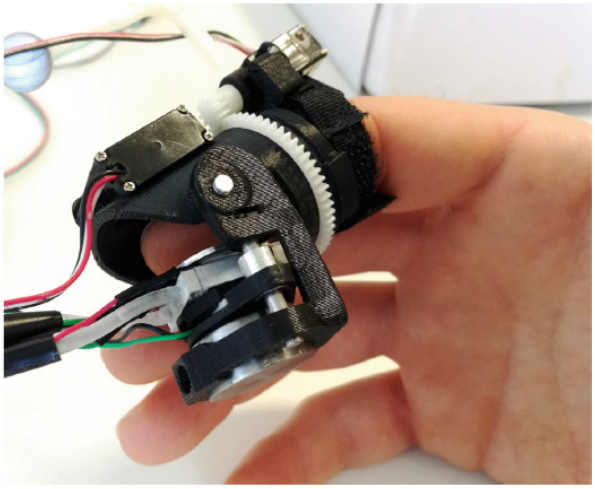

Figure 1.2: Realised prototype of thermo-electric haptic device, using liquid cooled Peltier elements [9]

Figure 1.2 shows a recent attempt to create a thermal haptic device. It uses water cooled Peltier elements that can be moved to come into contact with the fingertip. The Peltier elements can be mechanically moved to different sections of the finger. This setup achieved a response time of 1 second for a temperature step of 10 C (from 24 C to 14 C). Figure 1.2 also gives an indication of the dimensions of the setup and the components that are used. It can be seen that this setup takes up a lot of space, especially considering this system is for one finger only. The Peltier elements need to be water cooled due to its low efficiency. The large power consumption and heat load make Peltier elements difficult to incorporate into a wearable system.

In the process of creating a device that can create thermal feedback it is important to know the thermal properties of the hand and to know how temperature is perceived by the brain. As mentioned previously this field of research is relatively new and as a result the knowledge about human temperature perception is limited. This partly results from the paradox created by the fact that we need accurate thermal haptic devices to test temperature perception but in order to design these devices we need to know how temperature is perceived [8]. A way to bypass this paradox is to leave out the human factor and design a system that can create similar thermal behaviour as real life objects. How this is perceived by humans can be tested afterwards. For example, if the thermal behaviour of piking up a cold glass of lemonade is known this information can serve as an input for the control system. The thermal device in contact with the finger will have to mimic this known thermal behaviour, if this succeeds we may expect the user to have a realistic experience.

When it comes to the thermal properties of the hand we are not completely in the dark. Research has shown that when two thermal stimuli are presented on the same fingertip, participants were not able to discriminate between them even though they were able to discriminate between them quite reliably when the thermal stimuli were presented on two fingers of opposite hands [28]. As a result it will not be useful to have more than one thermal element per fingertip. Properties needed for the simulation of a finger such as heat capacity, conductivity and volumetric heat generation are known, albeit with significant variation between people [4]. Research has also been performed on the contact interface between finger and solid objects, this has yielded insight in the thermal resistance at the interface as a function of grip force [27]. As a result the thermal interaction between finger and solid can be simulated with reasonable accuracy.

In recent years first concepts capable of providing hot and cold sensations to the finger have been made. They proved the effectiveness of several systems and provided a basis for future research. A way to continue this research is to design a next generation thermal haptic device based on the thermal interaction between the finger and solid objects. A more in-depth research on this thermal behaviour could yield a device that is capable of more realistic sensations. This way the previously mentioned paradox can be bypassed by focusing on providing the most accurate thermal sensation. How the human body perceives this could be interesting follow-up research. In the previous paragraphs the challenges accompanied by the Peltier elements have been indicated. Instead cooling the Peltier elements with water the water can be used directly, which is the scope of this research.

The central research question in this research is:
How can realistic thermal behaviour be achieved with a liquid based thermal haptic device ?

The research question is sub-divided into smaller sub-questions which have been listed below.

- What should the geometry of the thermal haptic device look like ?
- How can the thermal interaction between finger and solids be modeled ?
- What relation exists between the input parameters and the thermal output of the device?
- Is it possible to control the device to create the desired thermal performance ?

In the following chapter the problem is defined more concrete including a study of the governing equations. In the subsequent chapter a start is made with 2D and axi-symmetric simulations which serve to characterise the thermal behaviour. This is followed by a dimensionless study in chapter 4. In the following two chapters regular PID control and Model Predictive Control are evaluated on a simplified model. In chapter 7 a start is made with the optimization of the full 3D geometry. Followed by recommendations discussion in chapter 8 and the conclusions in Chapter 9.

2 Problem definition

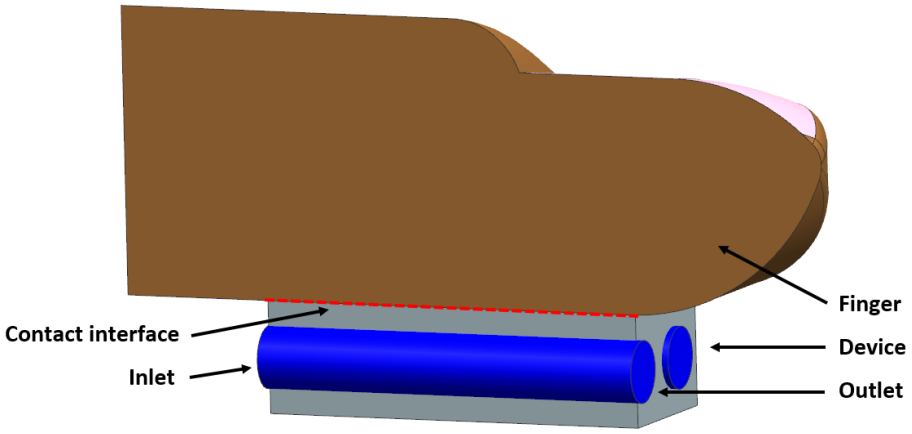

Figure 2.1: Cross section of a finger in contact with a thermal haptic device.

Figure 2.1 shows the cross section of a human finger in contact with a thermal device containing channels. Water is pumped through these channels, by changing the temperature of the incoming water thermal sensation can be produced on the surface of the finger in contact with the device. The main focus of the research will lie on the contact interface and how different designs and inlet conditions affect the temperature at the contact interface.

A good example to characterise these sensations is the action where you pick up a cold glass of milk. The cold sensation is felt almost instantly and gradually decreases in time. Ideally this research will yield a design that is able to recreate this rapid transient thermal behaviour.

To confine the problem several assumptions are made. The flow regime will remain laminar at all times, this is possible as the diameter of the channels are in the order of several millimeters. Inlet parameters are adjusted to ensure that the Reynolds number remains well below 2300. Equation 2.1 shows the expression for the Reynolds number, it represents the dimensionless ratio between the inertial forces in the numerator which are a product of the density, velocity and diameter compared to the viscus forces. If this ratio is above 10.000 it the inertial forces are dominant which will result in turbulence. When the ratio is below 2300 it can safely be assumed that the flow regime is laminar. The region in between contains both laminar and turbulent characteristics, and is therefore especially difficult to model. [21]

$$Re = \frac{\rho \cdot u \cdot d}{\mu} \tag{2.1}$$

The finger is modeled as a single isotropic material. In real life the finger is not homogeneous but is made up of several layers of tissue, blood vessels and bone. The first millimeters of the skin however is made of fatty tissue which has relatively constant thermal properties. A characteristic that defines this layer is its low conductivity, creating large gradients in the presence of a heat flux. As a result the core temperature of the finger remains approximately constant, this assumption is further strengthened by the comparatively short timescales of the thermal sensations. This justifies the assumption for the usage of a single isotropic material to simulate the finger.

Another key feature that has a major influence on the heat transfer is the interface resistance between the finger and the device. This contact is not perfect and thus creates a thermal resistance. The implementation of this interface resistance is elaborated in following paragraphs.

2.1 3D geometry

A 3D design of the thermal haptic device is shown in figure 2.2a. This specific design contains 4 channels. However the ideal number of channels is part of the design problem. The contact area between finger and device is kept constant at 15 x 15 mm. Dimensions that can vary are height h, diameter d and number of channels n. When the size of the channels is reduced it is possible to increase the number of channels. In evaluating the performance of two designs it will be difficult say what the relative influence was of the number of channels and the size of the channels when both parameters are changed. It is difficult to vary only one parameter at a time.

In order to make more general and useful conclusions from the results, the design in figure 2.2a is replaced by the design in figure 2.2b, this effectively is an approximation to the full 3D design. Here the only parameters that are variable are the diameter d and height h. Instead of changing both parameters only d is changed. By doing so the ratio between d and h is changed, this dimensionless ratio tells something about the relative thickness of the wall compared to the diameter of the channel. It is this dimensionless ratio that is of special interest as it is expected to have a significant influence on the heat transfer and resulting temperature distribution.

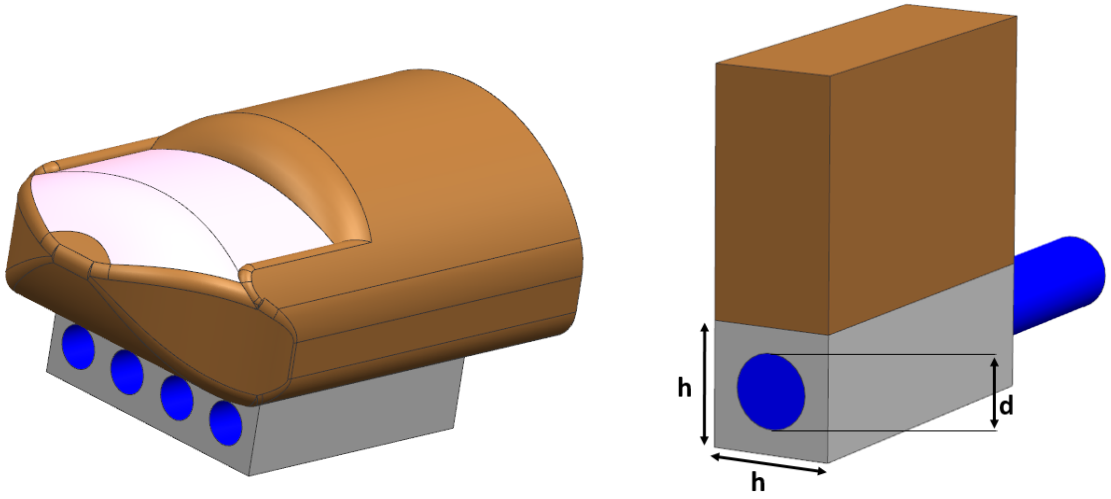

(a) Finger in contact with thermal haptic device

(b) Simplification of finger in contact with thermal haptic device

Figure 2.2: 3D geometries

2.2 Material choice

It is important to select an suitable material for the thermal device. A first characteristic that comes to mind is a low thermal resistance or high thermal conductance. From the common engineering materials copper has the highest conductivity. A disadvantage of copper is that it has a high density what can result in large mass of the device. This in turn can disturb the experience of the end user. Another suitable engineering material is aluminium, this strong light weight material is commonly used in heat sink applications. In steady-state, high conductance would be the most important thermal parameter, in transient simulations however this not definitely the case as here the thermal inertia will be the more important characteristic that influences the performance. The objective in this research is that the device change temperature fast between different set-points, this implicates the desire for a low thermal inertia. Which is dictated by the combination of parameters indicated below.

$$I = \sqrt{\rho \cdot k \cdot C_p} \tag{2.2}$$

Based on this metric copper performs only 9% better than aluminium. The advantages that aluminum is much easier to machine, has a density only 30% that of copper and is much cheaper creates a clear preference for aluminium.

2.3 Constraints

Before starting the simulations it is useful to acquire a general understanding in the limitations of the system. Either in the form of machining constraints that affect the geometry or considerations that effect the imposed boundary conditions in the simulations.

Wall thickness

The minimum thickness for the wall depends on the material as well as the machining process. When considering aluminium in combination with conventional CNC machining a minimum wall thickness as low as 0.8 mm can be achieved [5]. It is important to mention that this is absolute minimum and does depend on some other parameters of the geometry, such as its overall stiffness and how well it can be clamped in the machine. In regards to this absolute value, the constrained for the minimum wall thickness will be set at 1mm to ensure that it will comply with the machining constraints

Channel diameter

Suitable techniques for the manufacturing of the channels include conventional drilling and small hole edm. With both techniques it will be possible to make channels with a diameters as low as 1mm. It is possible to create even smaller channels, but this is accompanied by several problems and risks. A rapidly increasing pressure drop as well as reduced structural integrity.

Inlet velocity

The constrained on the inlet velocity is more based on a trade-off than a hard constraint. An increasing inlet velocity will increase the pressure drop and thus the power required to pump the liquid. In order to make this trade off more information regarding the complete fluid system needs to be known.

In this section the preliminary idea for the complete wearable system will be elaborated. The idea is that the user will carry reservoirs full of water pre-cooled and heated at the desired temperatures. Both reservoirs have a separate feed line that runs to the hand where the thermal devices are present, the two fluids are mixed just before they enter the device. As a first idea to power this system and control the mixing, each separate feed line is powered with a small fixed displacement pump. This creates the advantage that it will be relatively easy to control the flow and mixing as for each revolution of the pump the amount of displaced fluid is known. A sketch of this is shown in figure 2.3. Two feed lines are shown, one for the hot and one for the cold fluid, the green line indicates the return line.

Figure 2.3: user sketched with liquid setup, (red) hot fluid feed line, (blue) cold feed line, (green) return line

From this preliminary sketch a first assumption of the total pressure loss in the piping can be made. This estimation is made for one arm where at the hand 5 devices will be installed, one at each finger. The estimation is made using equation 2.3. Friction factor f can be determined exact for laminar flow or approximated by several empirical relations when turbulent flow is present. The friction factor for laminar is found with equation 2.4. For most bends, valves, in and outlets a K-factor is known, which can be used in equation 2.3. It is hard to determine the exact number of bends and shapes, however a first approximation is elaborated in table 6.1. Here the thermal devices, its inlets and manifolds are not considered.

$$\Delta p = \left(f \frac{L}{D} + \sum K \right) \frac{1}{2} \rho v^2 \tag{2.3}$$

$$f = \frac{64}{Re} \tag{2.4}$$

Table 2.1: Friction factors

	K-factor	amount	total
Inlet	1,0	1	1
Outlet	1,0	1	1
Bend 90	0.31	2	0.62
large bends	0.22	4	0.88
T-joint	0.69	1	0.69
Total			**4.19**

The inside diameter of the feed lines is set at 1cm, the length of the piping system is 1.5 m for the feed line and 1.5 m for the return line. For the calculations of the pressure loss it is assumed that only hot water or only cold water is pumped. This is the worst case scenario at which the pressure loss will be greatest. This is the pressure each pump will have to be able to supply at peak demand. Since most values in equation 2.3 are known it can be rewritten to the following form. Where v denotes the velocity in the lines.

$$\Delta p = 960v + 2095v^2 \tag{2.5}$$

The power consumption one pump will have to supply can be found using the equation 2.6. It should be noted that this power is the fluid power, the pumping power will be higher due to the losses inside the pump. Due to the small size of the pump the efficiency of the pump will be low, an efficiency of 50% is assumed. The pressure losses in the device including its manifolds are not known and are assumed to be of comparable order to the entire piping system.

$$P = \frac{\pi}{4}(0.960v^2 + 2.095v^3) \tag{2.6}$$

The before mentioned assumptions of the efficiency of the pump and losses in the device transform equation 2.6 into 2.7. Here it can be seen that even for velocities of 10-20 cm/s in the feed line the power consumption is of the order of several watts. It should be noted that this is the power consumption for one hand using 5 thermal devices and for a complete system this number needs to be doubled.

$$P_{total} = \pi(0.960v^2 + 2.095v^3) \tag{2.7}$$

When a velocity of 20 cm/s is used a volume flow of 15.7 ml/s is reached, which can be used for one hand consisting of 5 element. This creates a budget of 3 ml/s for each separate device. By doing so the Reynolds number in the piping system stays low enough to assume laminar flow, which is an advantage from an engineering perspective. The Reynolds number will reach 2000 in the feed line for a velocity of 20 cm/s.

Due to the low volume flow the pressure drop will not be expected to create significant power demand. The constrained that is constructed limits the volume flow of each device to 3 ml/s. Which is a useful and reasonable engineering value.

Inlet temperature

In order to construct constraints on the the inlet temperature it is useful to examine the thresholds for human pain reception. By setting limits on the minimum and maximum temperature in the system the safety of the end user can be ensured. Human pain receptors start to become active for temperatures below 15 C or above 45 C [7]. Tissue damage can occur when temperature below 0 or above 50 C are reached [7]. For this research it is chosen to constrain the inlet temperature by 0 C and 50 C to ensure that under no circumstance tissue damage can occur. With these limits it is however possible to create moderate pain sensations. It is order to apply some nuance to the previous statement. The lower threshold for pain sensation is 15 C, this implies that it is possible for some people to experience pain sensations when picking up a cold glass of beer with a temperature of 5 C. These sensations are mild and can not result in tissue damage.

The temperature of the incoming fluid will change in time, the speed with which this can be achieved is finite. Sharp changes will also be dampened by conduction in the fluid. However in this research no constrained is placed on the speed with which the inlet temperature can change, this is done to confine the problem at hand. It is possible that some inlet temperature profiles shown in this research are particularly difficult to create in real life, which could be an interesting subject in future research.

2.4 Governing equations

Flow

For the flow the two governing equations are the incompressible Navier-Stokes equation and continuity equation, shown in equation 2.8 and 2.9 respectively. This creates 4 equations for 4 unknowns, (v_x, v_y, v_z, p) three velocity components and the pressure. Incompressibility can be assumed since the velocities and pressures are low. The temperature differences are low, it is therefore reasonable to assume that the values for specific heat, thermal conductivity and viscosity are constants as well.

$$\rho\frac{\partial \mathbf{v}}{\partial t} + \rho(\mathbf{v}\cdot\nabla)\mathbf{v} = -\nabla p + \eta\nabla^2\mathbf{v} + \rho\mathbf{g} \tag{2.8}$$

$$\nabla\cdot\mathbf{v} = 0 \tag{2.9}$$

The variables in equation 2.8 and 2.9 can be substituted with the following relations for the dimensionless quantities. All velocity components are non-dimensionalised with the inflow velocity, the same principle applies to the 3 spatial dimensions that are made dimensionless using the diameter of the channels. U_s is the average inlet velocity, D_s is the diameter of a channel, p_s is atmospheric pressure $(10^5 Pa)$, t_s is found from a combination of the characteristic length and velocity.

$$\mathbf{u}^* = \frac{\mathbf{u}}{u_s}, \quad \nabla^* = \frac{\nabla}{D_s}, \quad p^* = \frac{p}{p_s}, \quad t_s = \frac{D_s}{U_s}, \quad t^* = \frac{t}{t_s} \tag{2.10}$$

When the expressions in equation 2.10 are substituted into equation 2.8 and 2.9 the following equations can be found that now only contain non-dimensional quantities.

$$\frac{\partial \mathbf{u}^*}{t^*} + (\mathbf{u}^*\cdot\nabla^*)u^* = -Eu\nabla^* p^* + \frac{1}{Fr^2}g* + \frac{1}{Re}\nabla^{*2}u^* \tag{2.11}$$

$$\nabla^* u^* = 0 \tag{2.12}$$

Three non-dimensional groups emerge, Euler number (Eu), Froude number (Fr) and the Reynolds number (Re). The solutions to equation 2.11 now only depend on the values of these groups. Since incompressibility applies the contribution of gravity translates into a hydrostatic pressure contribution. As a result both the pressure term and gravitational term in equation 2.11 are incorporated into the pressure term of equation 2.13

$$\frac{\partial \mathbf{u}^*}{t^*} + (\mathbf{u}^*\cdot\nabla^*)u^* = -Eu\nabla^* p^* + \frac{1}{Re}\nabla^{*2}u^* \tag{2.13}$$

To simplify equation 2.13 further the Euler is fixed at 1, thereby scaling the pressure term with the factor Eu. Due to the assumed incompressibility the pressure term has no thermodynamic contribution. The only variable left in the Navier-Stokes equation is the Reynolds number.

Heat

For the heat equation the same method is applied. The starting equation is the transient heat equation and Fourier‘s equation for heat conduction.

$$\rho C_p\frac{\partial T}{\partial t} + \rho C_p\mathbf{u}\cdot T - \nabla\cdot\mathbf{q} = 0, \qquad \mathbf{q} = k\nabla T \tag{2.14}$$

The temperature is non-dimensionalised using the expression 2.15. T_{min} and T_{max} are 0 C and 50 C respectively, as set by the constrained determined in section 2.3.

$$T^* = \frac{T - T_{min}}{T_{max} - T_{min}} \tag{2.15}$$

Substituting the expressions in 2.10 and 2.15 into equation 2.14 will yield the following dimensionless equation.

$$St\frac{\partial T^*}{\partial t^*} + \nabla^* T^* + \frac{1}{Re}\frac{1}{Pr}\nabla^{*2}T^* = 0 \tag{2.16}$$

In similar fashion to the Euler number the Strouhal number is set to 1. By doing so the characteristic time scale is determined, equation 2.16 illustrates how this time scale τ is defined. The only variable present in equation 2.16 is the combination $Re \cdot Pr$ also known as the Peclet number.

$$St = \frac{D_s}{U_s \cdot \tau} = 1, \qquad \tau = \frac{D_s}{U_s} \tag{2.17}$$

2.5 Boundary conditions

The application of the boundary conditions is visualised in figure 2.4. The sketch is a cross section of the geometry shown in figure 2.2b. The brown section represents the finger in contact with the device in light grey, the internal channel is filled with water indicated by blue. The contact interface is shown with the dashed red line. The conditions applied here are applied in the 2D and axi-symmetric geometry in similar fashion.

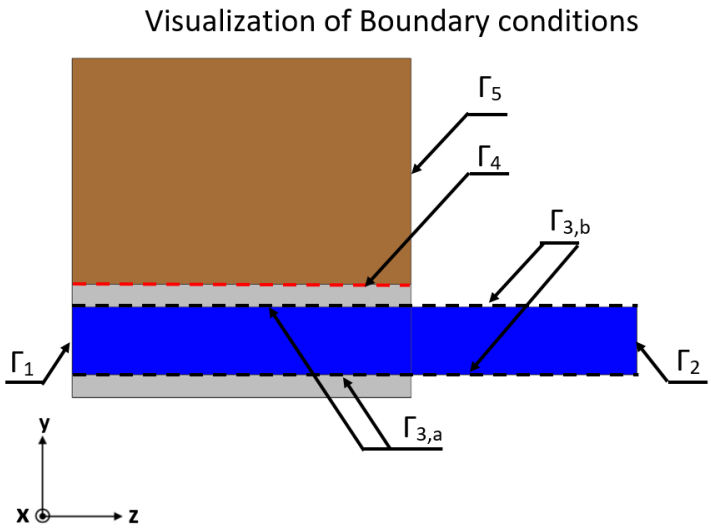

Figure 2.4: Visualisation of boundary conditions

Inlet

In some special conditions it is possible to find a exact solution to the Navier-Stokes equation. In fully developed pipe flow the Navier-Stokes equations reduce to the Poiseuille flow. This resulting parabolic velocity profile is shown in equation 2.18, where U denotes the maximum velocity, r denotes the radial coordinate of the channel and R denotes the radial dimension of the channel. This velocity profile is prescribed at the inlet indicated by Γ_1 in figure 2.4. The boundary condition for the prescribed velocity at the inlet is expressed in equation 2.19

$$V = 2U\left(1 - \left(\frac{r}{R}\right)^2\right), \qquad U = \frac{\Delta p R^2}{8\mu L} \tag{2.18}$$

$$[v_x, v_y, v_z]|_{\Gamma_1} = [0, 0, V], \tag{2.19}$$

In dimensionless form the inlet velocity can be expressed according to equation 2.20

$$V^*|_{\Gamma_1} = 2(1 - r^{*2}), \qquad r* = \frac{r}{R} \tag{2.20}$$

At the inlet a uniform inflow temperature is prescribed which is only a function of time. This boundary conditions is shown in equation 2.21

$$T_{in}|_{\Gamma_1} = T_{in}(t), \qquad T^*_{in}|_{\Gamma_1} = \frac{T(t) - T_{min}}{T_{max} - T_{min}} \tag{2.21}$$

Outlet

At the outlet the gradients of the velocity and temperature are set to zero according to 2.22, the pressure is zero at the outlet. The zero gradient condition may influence the solution as in real life gradients can be present at a outlet. To prevent the influence of the zero gradient boundary conditions on the solution the outlet is lengthened, which can be seen in figure 2.4. The boundary conditions for the outlet are elaborated in equation 2.22, where n denotes the direction perpendicular to the outlet.

$$\left.\frac{dT}{dn}\right|_{\Gamma_2} = 0, \qquad \left.\left[\frac{dv_x}{dx}, \frac{dv_y}{dy}, \frac{dv_z}{dz}\right]\right|_{\Gamma_2} = [0,0,0], \qquad p|_{\Gamma_2} = 0 \tag{2.22}$$

Channel wall

The wall of the channel is divided in a section in contact with the device $\Gamma_{3,a}$, and section $\Gamma_{3,b}$ not in contact with the device. For the entire wall a no-slip condition applies according to equation 2.23.

$$[v_x, v_y, v_z]|_{\Gamma_{3.a-b}} = [0,0,0] \tag{2.23}$$

For the section in contact with the aluminum device a thermal boundary condition applies according to equation 2.24. This conditions equates the two heat fluxes on both sides of the wall, where k_f denotes the thermal conductivity of the fluid and k_s indicates the thermal conductivity of the solid material of the device, n denotes the coordinate normal to the channel wall.

$$\left.\left[k_f \frac{dT}{dn}\right]\right|_{\Gamma_{3.a}} = -\left.\left[k_s \frac{dT}{dn}\right]\right|_{\Gamma_{3.a}} \tag{2.24}$$

On the section of the wall not in contact with the device, denoted with $\Gamma_{3,b}$ an adiabatic condition is applied according to equation 2.25.

$$q = k_f \left.\frac{\partial T}{\partial n}\right|_{\Gamma_{3,b}} = 0, \qquad \left.\frac{\partial T^*}{\partial n^*}\right|_{\Gamma_{3,b}} = 0 \tag{2.25}$$

External walls

The heat loss to the ambient air is assumed to be much smaller than the internal heat flux. Therefore the external walls in contact with the ambient denoted by Γ_5 are assumed to be adiabatic. This is expressed in equation 2.26.

$$q = k \left.\frac{\partial T}{\partial n}\right|_{\Gamma_5} = 0, \qquad \left.\frac{\partial T^*}{\partial n^*}\right|_{\Gamma_5} = 0 \tag{2.26}$$

Contact interface

The finger and device are not fully in contact over the entire contact area Γ_4. Due to the surface roughness the finger is only partly in contact with the metal device. This is shown in figure 2.5a. Research on this subject has made it possible to characterise the interface resistance between the finger and varying materials. This interface resistance is a function of the applied grip force. The grip force will deform the surface of the finger thereby increasing the contact area, resulting in better heat transfer.

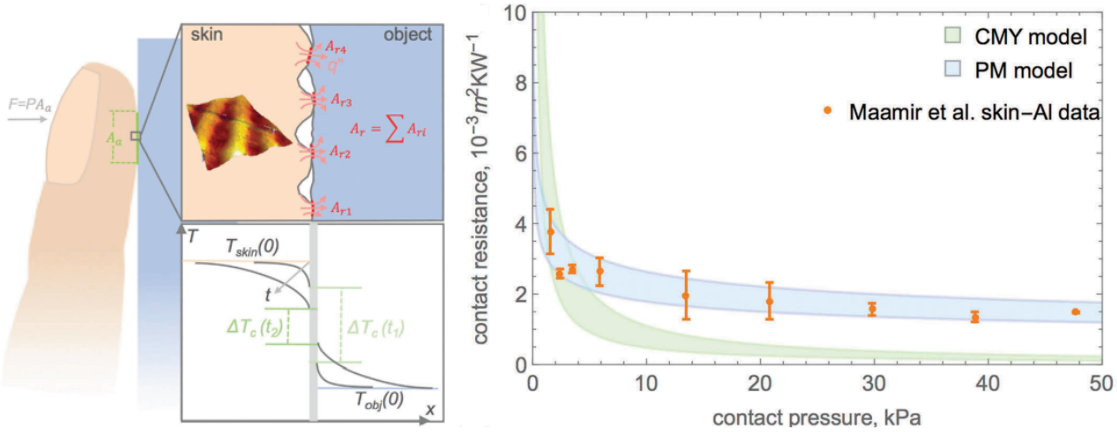

(a) Interface contact [27]

(b) Interface resistance for finger-aluminium contact [27]

Figure 2.5: Interface properties

From figure 2.5b it can be seen that the experimental results for the interface resistance appear to approach constant value of $0.002 m^2K/W$ for contact pressures of 5 kPa and upwards. This value will be used in all simulations.

An important consequence of the interface resistance is resulting discontinuity in the temperature field perpendicular to this interface. This effect is visualised in figure 2.5a, the size of this discontinuity is proportional to the heat flux moving through this interface. The temperature just above the interface om the side of the finger is denoted with T_f in equation 2.27, T_d denotes the temperature at the side of the device. The dimensionless interface resistance R_i^* is the product of the resistance, the thermal conductivity of aluminium k_a and the wall thickness t_w.

$$R_i|_{\Gamma_4} = \frac{q_i}{T_f - T_d}, \qquad R_i^* = R \cdot k_a \cdot t_w \tag{2.27}$$

Interface temperature definition

Due to the discontinuity it is important to make a clear definition on how the interface temperature is defined. In this research the interface temperature will refer to the temperature at the side of the device. In figure 2.5a this corresponds the temperature at the right size of the contact interface. It is important to note that when the interface temperature reaches a desired set-point of, for example 10 C, this does no imply that the finger has reached this value.

2.6 Methods

The complexity of the problem makes it not possible to find an analytical solution. In order to acquire meaningful results the transition is made to numerical analysis. Here the geometry is discretised into finite volumes. The conservation equations for momentum, mass and energy shown in equation 2.8, 2.9 and 2.14 are solved for each finite volume, this enables the conservation of fluxes moving through the control volume. The equations are solved iteratively until a set value for the residuals is reached, this process is repeated for each time step in the simulation.

Software

The problem contains a combination of transient heat transfer in laminar flow and heat transfer in solids. A suitable and recognised software package specialised in multiphysics simulation is COMSOL. The simulations will all be performed using this software.

Mesh

The geometry is discretised by the mesh, this mesh mush be fine enough to capture the gradients of relevant parameters, however an increasingly fine mesh also increases the number of computations that have to be performed. In 3D the number of elements increased in a cubed fashion when the mesh is refined. When the size of the elements is halved the number of elements increases by a factor of 8, this rapidly increases the computational cost of the simulation. The mesh must be fine enough to ensure that the spatial gradients can be captured. The problem consists both of solid and fluid mater. This fluid is in motion and the velocities here are dependant on the imposed boundary conditions. In turn the spatial gradients in the velocity field vary depending on the imposed boundary conditions, most notably the imposed mass flux at the inlet of the system. As a consequence special care has to be taken to ensure the mesh is always fine enough, if boundary conditions are changed.

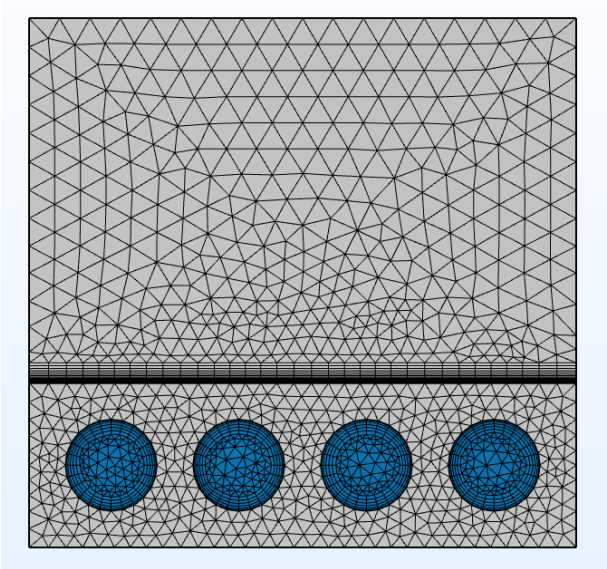

Figure 2.6: Mesh

Special elements in the mesh are the so called boundary layers. These are thin layers of mesh where the size of the mesh grows exponentially. The first layers are very thin and are therefore suitable to capture steep gradients. This is most often used in fluid domains, on the fluid-solid contact, where boundary layers are present and large gradients emerge. Another specific location where such elements are needed is on the contact interface on the side of the finger. The finger has poor thermal conductivity, it is therefore possible for large thermal gradients to occur. In figure 2.6 the boundary layers mesh elements can be seen in the fluid adjacent to the wall and at contact interface where the large thermal gradients are present.

2.7 2D & axisymetric problem definition

In the first stage of this research it is useful to acquire a general understanding of the relevant processes and relative importance of different variables. In order to do so it is useful to perform relative simple simulations that can be done in quick succession. A way to do so is to convert the 3D problem into a 2D problem. This greatly reduces the number of elements in the computation and thus reduces the computation time.

2D

It is important to note that the conversion from 3D to 2D is accompanied by several major simplifications and assumptions. This means that will not be possible to make exact translation between the results in 2D and 3D. However observed behaviour in 2D may be expected to appear in 3D. The general correlation between the variables and resulting temperature field can yield insight that can be helpful in the 3D simulations.

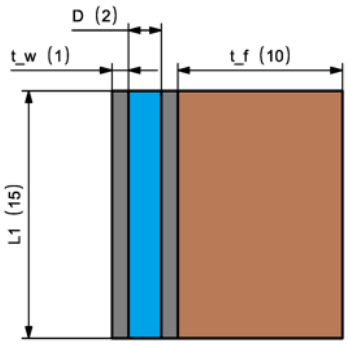

Figure 2.7: 2D problem sketch, finger (brown), device (gray), fluid (blue), dimensions in millimeter

In figure 2.7 the 2D problem is shown. It depicts a section of the finger in contact with a device containing one water filled channel. This is a simplification of the original problem shown in figure 2.1. The 2D nature of the simulation dictates that there are no gradients in the direction perpendicular to the 2D surface.

Axisymetric

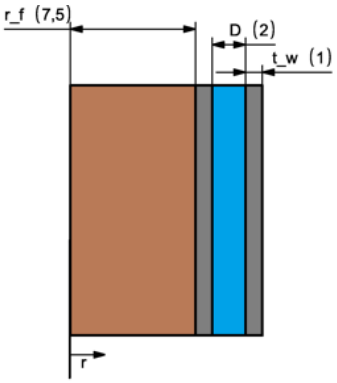

Figure 2.8: axisymetric problem sketch, finger (brown), device (gray), fluid (blue), dimensions in millimeter

As an intermediate step between the 2D and 3D, axisymetric simulations are performed. These simulations have a low computation load, comparable to that of the 2D simulations. However 3D characteristic are present. The main assumption here is that there are no gradients or velocities in the tangential direction.

3 Characterisation of thermal dynamics

In order to gain a thorough understanding of the thermal dynamics a start is made with 2D simulations. The short computation time of the 2D simulations create the opportunity to investigate a wide range of geometric configurations and boundary conditions. Observations made in these simulations will help gain insight as the complexity of the simulations increase during the research.

3.1 Heat production

The human body produces heat which is transported through the body using blood vessels. In simulating a finger in contact with a device it should be understood what the influence is of body heat production is on the thermal behaviour of the system. Previous research on the heat generation in human hands have yielded the value of 30 kW/m^3 [4]. Figure 3.1 shows two simulations using the geometry shown in figure 2.2b. Initially the temperature of the system is at 30 C, at t=1 s the inflow is changed to 0 C. In figure 3.1 the response of the interface temperature is shown both with and without the presence of a volumetric heat production term for the finger. The resulting response is almost identical, the maximum difference between the lines does not exceed 0.1 C. This minor difference does not make it useful to incorporate the heat production term in the simulations.

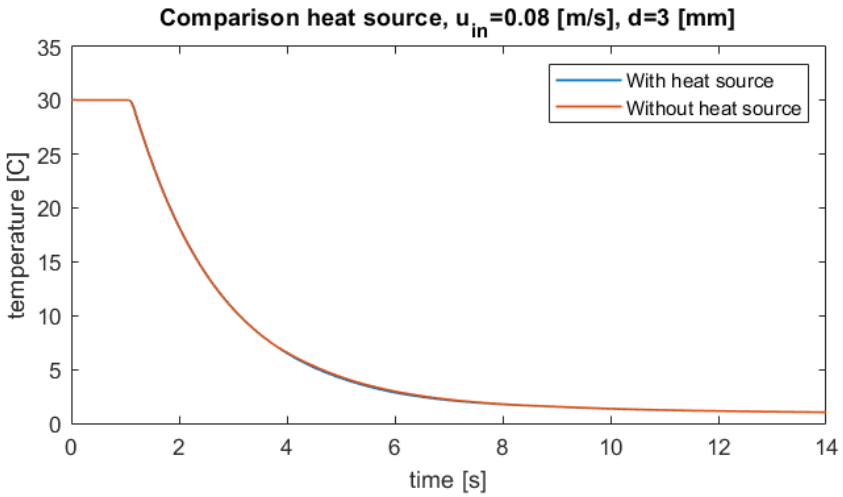

Figure 3.1: Negligible effect of incorporating volumetric heat production term of 30 kW/m3 in the finger

3.2 Internal temperature field

The focus of this research lies on the interface temperature and inlet temperature. These parameters can be visualised in a line plot such as figure 3.1. It can be useful to gain some intuitive understanding of the internal temperature field. Figure 3.2 visualises a simulation of the 2D geometry shown in figure 2.7. The interface temperature is plotted along with the internal temperature field for 4 instances. It can be observed that the aluminum walls of the device only contain very small gradients. The section representing the finger, on the other hand, exhibits large gradients perpendicular to the contact interface.

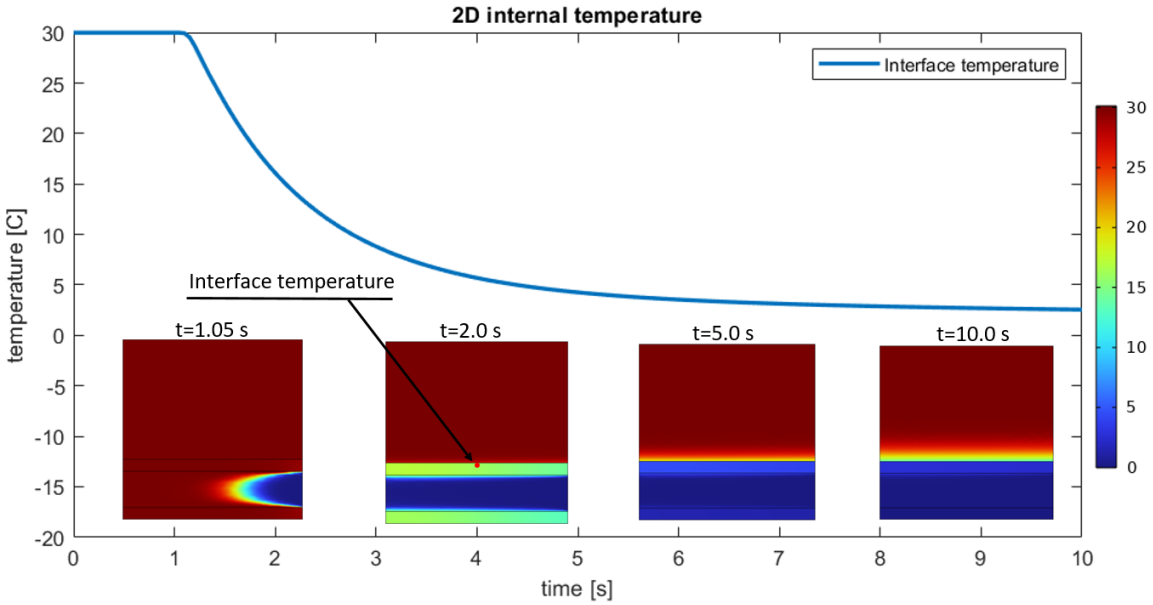

Figure 3.2: 2D internal temperature profile

As mentioned earlier, the interface temperature is defined slightly to the side of the device. This is a result from the discontinuity created by the interface resistance. Due to the high thermal conductivity of aluminium the temperature variations along the length of the device are minimal. It is therefore appropriate to define the interface temperature on the central point along this interface, indicated in figure 3.2.

Another consideration for using a single point instead of an average is the computational load. This is especially apparent in 3D simulations where the controllers are tested. If it is required for the controller to evaluate a surface averaged interface temperature for each time step, this will have a significant effect on the computational load. It is therefore more appropriate to define the interface temperature by the point indicated in figure 3.2.

It was observed that during the simulations of the 2D, axi-symmetric and 3D geometry the internal temperature distribution remains largely the same. The characteristics elaborated in this section using figure 3.2 return in almost every simulation. To prevent recurrence throughout the report not every section of the report is accompanied with figure containing the internal temperature distribution.

3.3 Linear system of equations

The temperature in the simulations varies no more than 50 C, which justifies the assumption that the material parameters are constant. The Reynolds number of the flow in the simulations is kept well below 2000 which creates a laminar flow field, which in combination with a constant flow velocity will create a linear system of equations. This implicates that the solutions of two different inlet conditions can be added or subtracted. This is tested in simulations where the inlet temperature follow a sinusoidal profile.

Figure 3.3 shows the observed temperature profiles at the contact interface as a function of time. The temperature of the incoming flow is varied sinusoidal according to equation 3.1. The green curve shows the resulting interface temperature for the simulation where the inlet temperature profile is the multiple of the red and blue inlet conditions. The same interface temperature profile can be achieved by superposition of the red and blue curves indicated by the black line, validating the hypothesis that the system of equations is linear. A similar outcome can be observed when examining block functions or any arbitrary function.

$$T_{in}(t) = A_1 \cdot sin(B_1 \cdot t) + A_2 \cdot sin(B_2 \cdot t) \tag{3.1}$$

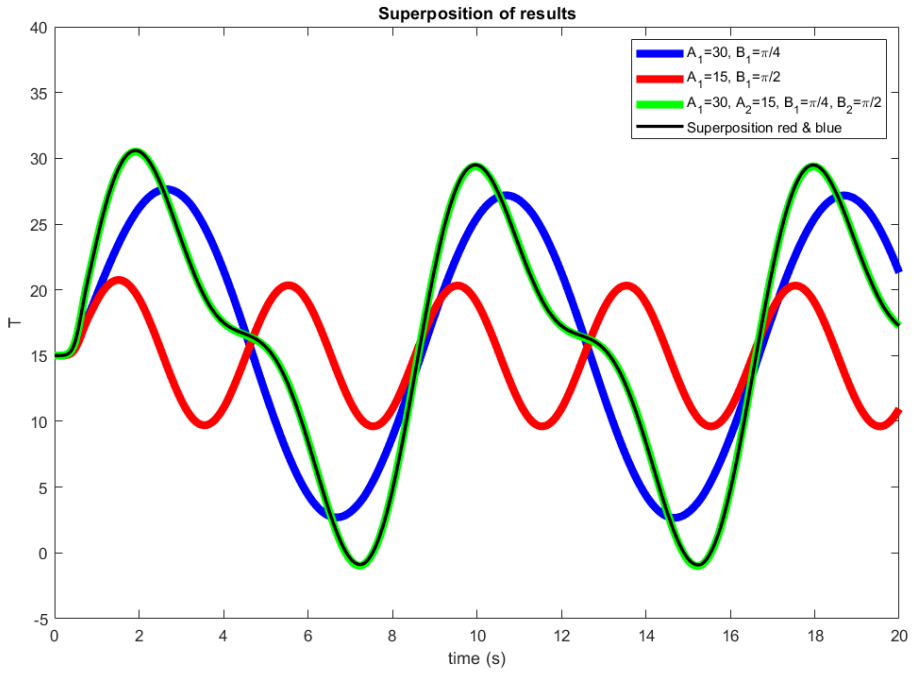

Figure 3.3: Superposition of simulation results, following a linear set of equations

$$T_1(g(t) + h(t)) = T_2(g(t)) + T_3(h(t)), \qquad T(T_{inlet}(t)) \tag{3.2}$$

The principle of superposition is shown in mathematical notation in equation 3.2. It shows how any temperature field T_1 can can be constructed from the superposition of independent simulations, where the argument of the functions represents the inlet temperature profile. A method particularly applicable here is the Fourier transform which states that any arbitrary signal can be represented by an infinite set of sines. If the response of the interface temperature is known for a range of sinusoidal inlet temperature profiles, the interface temperature can be constructed from the responses by means of superposition. The Fourier transform can be applied to determine series of sines needed to recreate the desired signal.

3.4 2D frequency analysis

In order to be able to construct a signal with sines by means of a Fourier series, it is required to know the response of the interface temperature for a range of frequencies. In this section the transfer between a sinusoidal inlet temperature and resulting interface temperature is examined. The inlet temperature profile is sinusoidal with an constant amplitude of 15 C, the frequency is varied between 0.05 and 0.5 hz. In total three different geometries introduced in table 3.1 are tested on a inlet velocity of 0.01 and 0.02 m/s.

For each geometry and inlet velocity the temperature behaviour at the contact interface is compared to the temperature profile at the inlet. The ratio between the amplitude of the interface temperature and inlet temperature is shown in 3.4a, the phase lag is shown in 3.4b. It can be observed that the amplitude measured at the interface decreases as the frequency of the inlet temperature is increased. This results from the thermal inertia of the system, the channel wall essentially acts as a low pass filter. Each design was tested on two different inlet velocities, the highest inlet velocity achieves the highest amplitude of the interface temperature for all frequencies. This can be explained by the higher mass flux and steeper thermal gradients in the fluid driving the heat flux. From the phase lag less general behaviour can be deduced, however the general trend in 4 of the 6 curves is that the phase lag approaches a constant value.

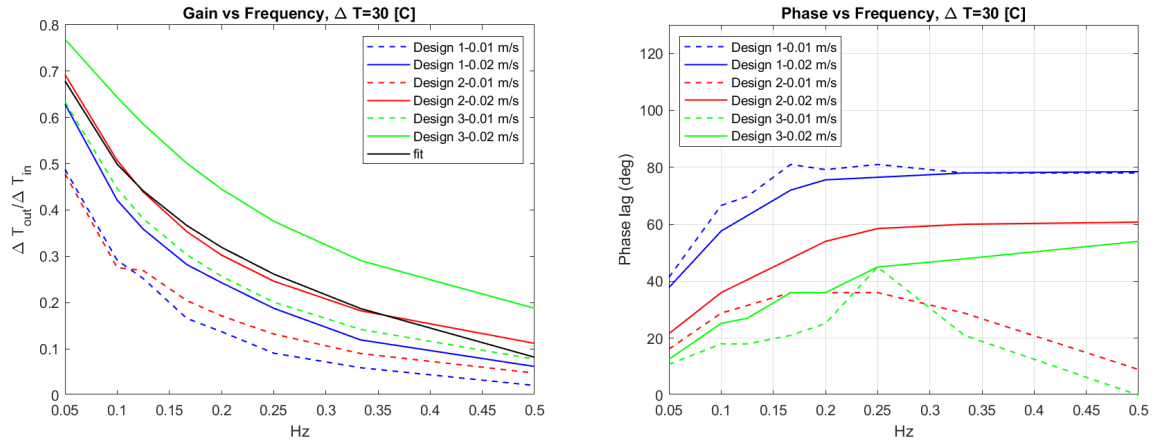

(a) Gain vs frequency

(b) Phase vs frequency

Figure 3.4: Transient behaviour

When looking at the data from the different geometries in figure 3.4a it can be observed that design 3, with the thinnest wall and smallest diameter has the largest transfer between the amplitude of the inlet temperature to the interface temperature over all frequencies. The worst transfer is observed for the design with the thickest wall and largest diameter. Both a reduction in channel diameter between design 1 and 2 and the reduction of wall thickness between design 2 and 3 independently increased the transfer between the inlet and interface temperature.

When the data form figure 3.4a is plotted on a semi logarithmic scale a linear trend can be observed. Using this knowledge the function shown in equation 3.3 is fitted where the variable f represents the frequency of the inlet temperature, parameters a and b are used to fit the function to the data. The resulting fit denoted by the black line shows good correspondence with the data in figure 3.4a.

$$fit = a \cdot log(f) + b \tag{3.3}$$

Table 3.1: Table

	Wall thickness [mm]	Channel diameter [mm]
Design 1	1	2
Design 2	1	1
Design 3	0.5	1

Step response

It has been shown that the temperature field is scalable according to equation 3.2. It is interesting to see if the temperature is scalable in time as well. In order to do so step responses are evaluated. In the following simulations the entire domain is initially at 30 C, at t=0 the inlet temperature is set at 0 C, the velocity remains constant for a given simulation. In total 3 geometries are simulated, the ratio between the wall thickness and diameter remains constant. Each geometry is simulated with 4 different inlet velocities, creating 12 different simulations in total.

The scope is to investigate to what extend the step response of the interface temperature is scalable in time, according to equation 3.4. Here a represents the scaling factor, T_b represents the base function used for scaling.

$$T_1(t) = T_b\left(\frac{t}{a}\right) \tag{3.4}$$

The interface temperature is evaluated and compared to the other step response simulations. This concept is shown in figure 3.5a where the blue curve is scaled in time to fit the red curve. From the 12 simulations one base response is selected and scaled in time to fit on the other simulations. The corresponding scaling factors are plotted in figure 3.5b, where planes are drawn between the 12 data points. The red dot indicates the base function that is used to scale the other step responses, this point corresponds to a diameter of 2 mm and inlet velocity of 0.08 m/s. The result is that, within an error margin of 1.5 C, all step responses can be scaled in time to fit a single step response. This analogy can be reversed, for a given geometry and inlet velocity the temperature response at the contact interface can be predicted with reasonable accuracy by finding the scaling factor corresponding to the inlet velocity and channel diameter in figure 3.5b. By doing so the data from the 4 nearest points is used to interpolate and find the appropriate scaling factor. The scaling factor a will, in combination with the base step response according to equation 3.4, give an approximation of any step response within the range of simulations seen in figure 3.5b.

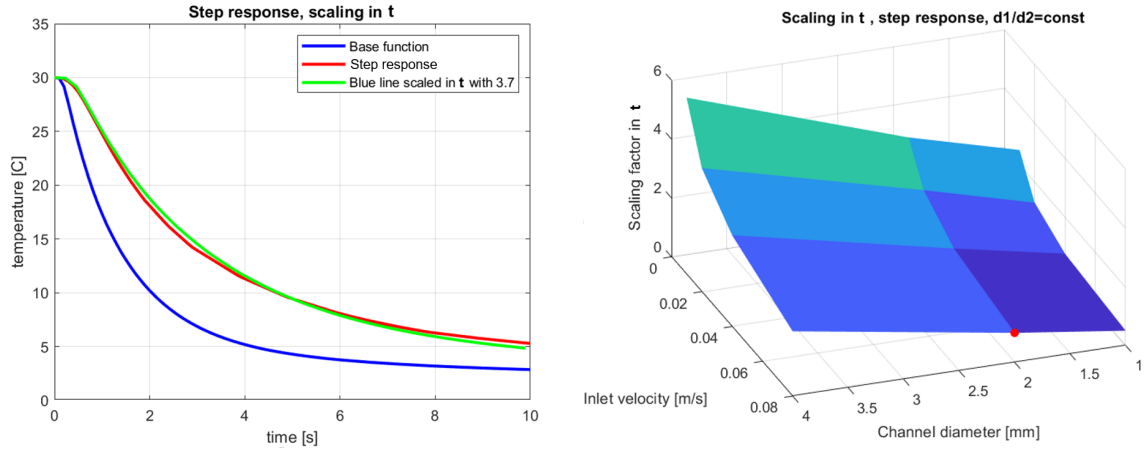

(a) Interface temperature vs time

(b) scaling factors

Figure 3.5: Scaling in x-direction

In the design of the thermal device it desirable that the interface temperature can change temperature fast. The blue line in figure 3.5a has a faster response that the red line. The fastest temperature response will correspond to the smallest scaling factor. When examining the plane in figure 3.5b it appears to have a convex shape with its minimum in the bottom right corner. This point has the smallest scaling factor and thus the fastest temperature response. This point belongs to the simulation with smallest channel diameter, wall thickness and the highest inlet velocity. The higher inlet velocity increases the available mass flow and thermal gradients which result in a faster response and therefore the scaling factor. The effect of reducing the channel diameter on the response time is less clear as the ratio between wall thickness and channel diameter was kept constant in the simulations. It can therefore not be said if the faster response is due to the reduction in diameter or wall thickness.

3.5 Axi-symmetric simulations

It is interesting to perform a similar analysis using axi-symetric simulations before a start is made with the 3D simulations. The computational load remains low in axi-symetric simulations, however 3D characteristics are present. In the problem definition in figure 2.8 the device is wrapped around a finger. Similar to the transient analysis in 2D, the transfer of the inlet temperature to the interface temperature is examined.

Frequency analysis

For the axi-symmetric simulations a sinusoidal inlet temperature is prescribed while the inlet velocity remains constant. The amplitude of the inlet temperature is 15 C and varies in frequency between 0.05 and 0.5 Hz. In the axi-symmetric analysis identical values for wall thickness and channel diameter are used. The corresponding axi-symmetric geometries can be found by implementing the values in table 3.1 according to figure 2.8.

Figure 3.6a shows the ratio between the observed interface temperature amplitude and inlet temperature amplitude. It can be observed that a similar trend can be observed compared to figure 3.4a. An increase in frequency will decrease the transfer between the inlet and interface temperature. Here logarithmic behaviour is observed as well, shown by the dotted logarithmic fit. The green curve has the best performance as the transfer between the inlet temperature and interface temperature is highest for all inlet frequencies. The observation indicates that thinner walls as well as smaller channels both increase the transfer of heat from the fluid to the contact interface. The phase lag observed in the temperature signal at the interface seems to approach a constant value as the frequency increases, a similar observation was made in the 2D analysis.

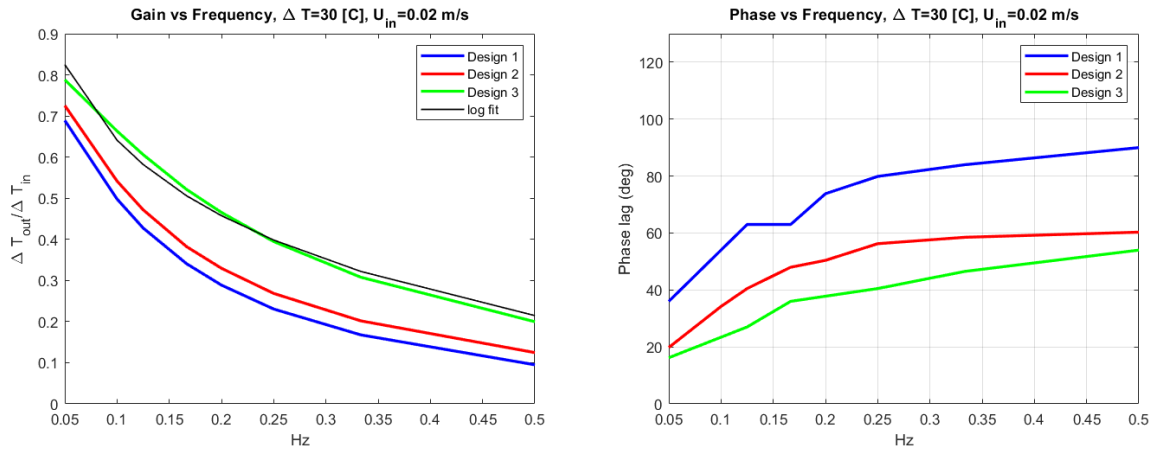

(a) Gain vs frequency

(b) Phase vs frequency

Figure 3.6: Transient behaviour in axi-symmetric simulations

Using either figure 3.6 or 3.4 a response can be constructed from the superposition of sines.

4 Dimensionless thermal characterisation

The 2D and axi-symmetric simulations have yielded interesting observations. In order to extend these observations and create a more thorough and general understanding this chapter will focus on a dimensionless characterisation of the step response of the thermal haptic device. Central in the dimensionless analysis is the approximation of the 3D model, which is introduced in figure 4.1.

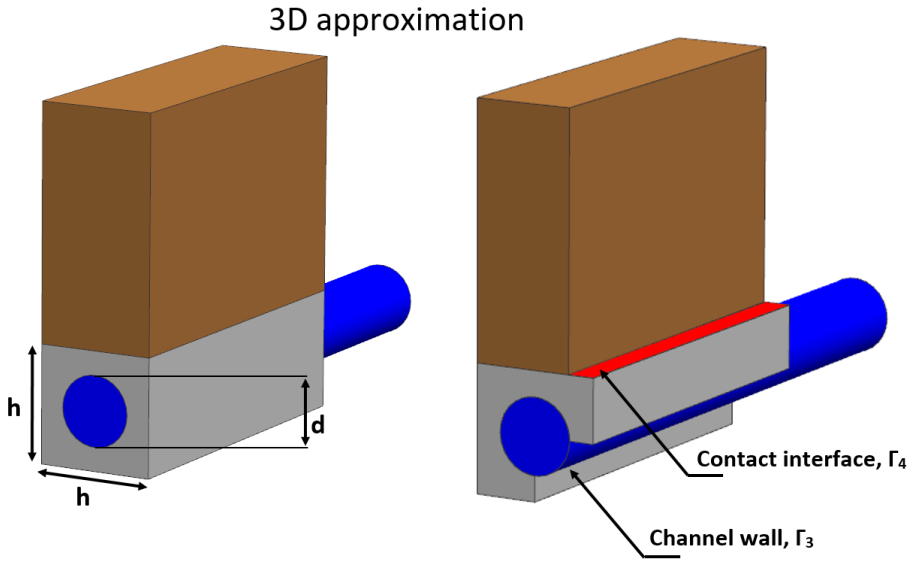

Figure 4.1: Sketch of 3D approximation

$$d^* = 1 - \frac{d}{h} \tag{4.1}$$

Chapter 3 has indicated in figure 3.4 and 3.6 that decreasing the wall thickness has a positive effects on the transfer between the inlet temperature and contact interface for 2D and axi-symmetric systems. This effect is further analysed in this chapter by means of a dimensionless analysis. The height h is used as the characteristic length to define the geometry. The ratio between the diameter d and height h is a first dimensionless parameter $d^{'}$, used to represent the dimensionless wall thickness. A small dimensionless wall thickness will correspond to a large value for $d^{'}$. To avoid confusion the expression for d^* is used in equation 4.2, here a low dimensionless wall thickness corresponds to a low value for d^*.

$$h^* = \frac{h}{h} = 1, \quad d^{'} = \frac{d}{h}, \quad d^* = 1 - d^{'} \tag{4.2}$$

The analysis of the governing equations has showed that the dimensionless heat equation shown in equation 2.16 is governed by the Peclet number. Therefore the Peclet number is the second dimensionless parameter that is varied in the simulations. The Peclet number for heat transfer is found by the product of the Reynolds number and Prandtl number according to equation 4.3, by varying inlet velocity and diameter Peclet numbers between 200 and 2000 are simulated.

$$Pe = Re \cdot Pr \tag{4.3}$$

All simulations consist of a step response, initially the system is at 30 C and at t=1 s the inlet temperature is changed to 0 C. With the simulations the dimensionless response time will be evaluated as well as the dimensionless heat flux trough the channel wall.

4.1 Response time

The inlet temperature changes with a a step from 30 C to 0 C, subsequently the interface temperature is evaluated. The time it takes for the interface temperature reach 50% of the step is defined as the response time, denoted by $t_{1/2}$. This corresponds to the time at which the interface temperature reaches 15 C. This response time is made dimensionless with characteristic diffusion time t_d according to equation 4.4. The channel diameter and diffusivity of water are represented with d and α_f respectively. The resulting dimensionless response time is denoted with $t^*_{1/2}$.

$$t^*_{1/2} = \frac{t_{1/2}}{t_d}, \qquad t_d = \frac{d^2}{\alpha_f} \tag{4.4}$$

Figure 4.2 shows the dimensionless response time for a range of Pe numbers and values for d^*. The dimensionless response time is represented on the z-axis. The resulting surface connecting the data points appears to have a convex shape. The shortest response time is found for the highest Peclet numbers and the lowest dimensionless wall thickness. This can be explained by the fact that by lowering d^* the thermal resistance of the wall is reduced, therefore a faster response can be observed. The Peclet number represents the ratio between the advective and conductive heat transfer. From figure 4.2 is can be deduced that the increased Peclet number has a positive effect of minimising the response time, which result from the increase in advective heat transfer by the flow.

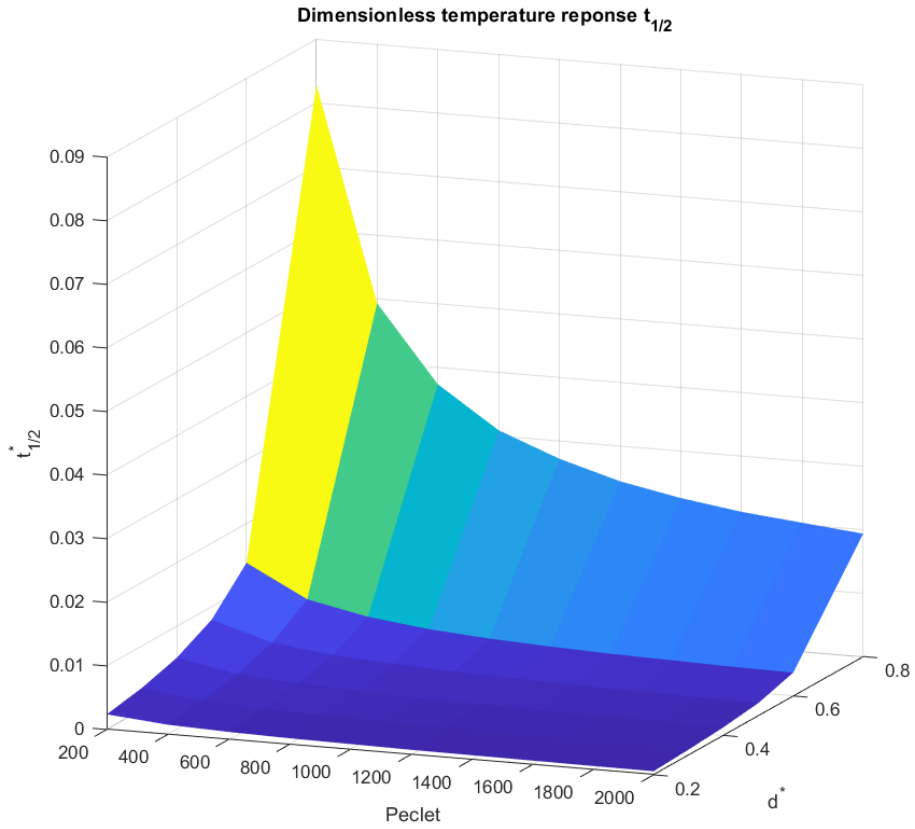

Figure 4.2: Dimensionless response time $t^*_{1/2}$

The minimum value for $t^*_{1/2}$ is constrained by the maximum Peclet number and minimum wall thickness d^*. However the effect of a change in Peclet number on the response time for the lowest dimensionless wall thickness appears to be minimal. Both the effect of increasing the Peclet number and reducing d^* on the response time diminishes as the minimum value is reached. The gradients of the surface plotted in figure 4.2 reduces for increasing values of Pe and lower values for d^*.

4.2 Effectiveness

For the same series of simulations the peak achieved heat flux magnitude in the channel wall Q_p is examined for each simulation. This result can be non dimensionalised with the maximum heat flux that can be achieved by the flow Q_{max}, expressed in equation 4.5. This maximum heat flux Q_{max} consists of the mass flow $\dot{m}$, heat capacity Cp and maximum temperature difference ΔT. The maximum temperature is the difference between the initial temperature of 30 C and inlet temperature of 0 C, which is constant for all simulation.

$$Q_{max} = \dot{m} \cdot Cp \cdot \Delta T \tag{4.5}$$

The measured peak heat flux Q_p is made non dimensional with Q_{max} according to equation 4.6. This ratio can be interpreted as the effectiveness of the device, also known as ϵ.

$$\epsilon = \frac{Q_p}{Q_{max}} \tag{4.6}$$

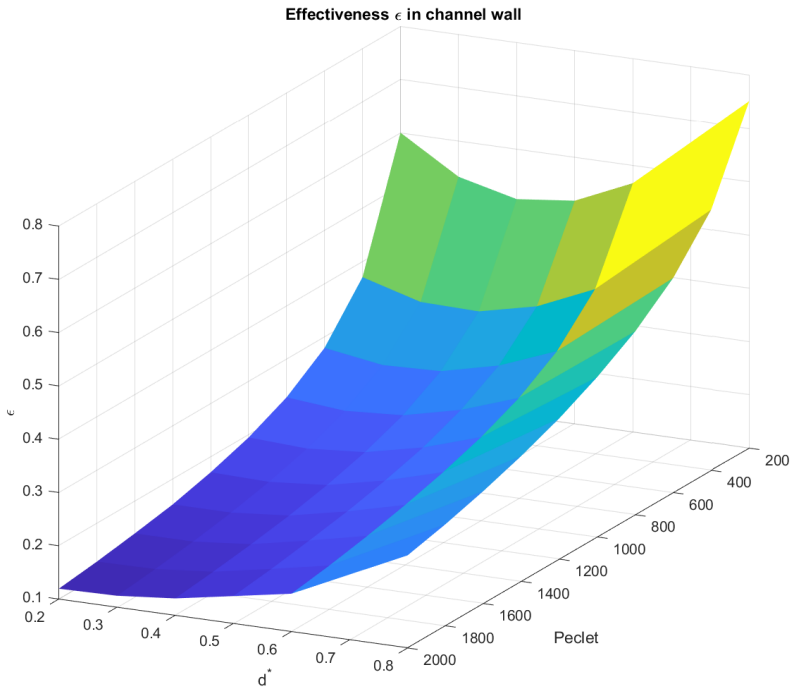

Figure 4.3: Dimensionless maximum heat flux magnitude across channel wall

The effectiveness is plotted on the z-axis. It can be observed that the minimum value for the effectiveness is achieved for the lowest dimensionless wall thickness and highest Peclet number. The effect of the change in d^* on the effectiveness follows from the fact that it changes the ratio between the fluid volume and the solid volume of the device from which the heat is extracted. The smallest values for d^* have a relatively small solid volume from which heat is extracted to a relatively large fluid volume. It therefore affects the peak heat flux and effectiveness according to 4.6. This effect is strongest for the simulations with higher Peclet numbers.

An explanation regarding the effect of the Peclet number on the effectiveness has not been elaborated. Instead the observed characteristics of the Peclet number in figure 4.3 have just been mentioned in the previous paragraph. Figures 4.2 and 4.3 provide a basic characterisation of the dimensionless behaviour. However a more in-depth interpretation of the results can be performed, which can be the scope of further research. If further analysis is performed, the dimensionless application of the interface resistance should receive extra attention. It was concluded afterwards that the dimensionless interfaces resistance varies in the simulations, which could influence the results discussed in this analysis.

5 PID control of the interface temperature

To simulate thermal sensations the interface temperature needs to be manipulated. To do so, some form of control strategy is needed. The first approach is PID control. This form of control is widely used in industry, because of its relative simplicity and robust control behaviour. The scope of this chapter is to acquire a first and general understanding of the possibilities of PID control applied to the thermal haptic device.

Figure 5.1 shows a schematic representation of a PID control loop. The input of the controller is the error signal e(t), which is the difference between the reference signal and measured output. In this case the measured output is the interface temperature. The controller consists of three distinct actions a proportional action, a integrating action and a derivative action. Each of these actions is multiplied with a gain, Kp represents the proportional gain, Ki the integration gain and Kd is the derivative gain. The reference signal is added to the controller output to ensure that a non-zero steady state can be achieved. The resulting control action u(t) is the inlet temperature for the CFD model in Comsol which can also be referred to as the plant. By changing the gains one is able to tune the PID controller to the desired characteristics.

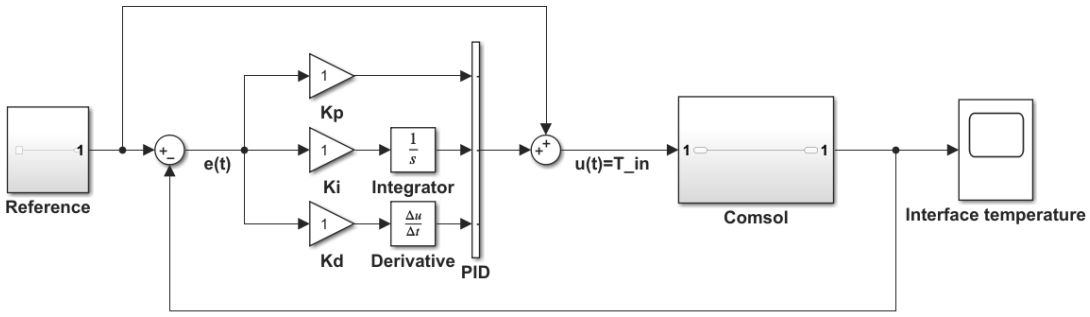

Figure 5.1: Schematic representation of PID control loop

The mathematical representation of the controller in figure 5.1 is shown in equation 5.1. In this research only the inlet temperature is varied, the inlet velocity remains constant. If the inlet velocity would need to be controlled as well this would require a new separate PID loop. Changing the inlet velocity has a large influence on the temperature behaviour, but the separate PID controllers have no knowledge of this effect. As a result such systems have poor control and can become unstable. Therefore in this research inlet velocity remains constant and only the inlet temperature is controlled.

$$u(t) = ref(t) + K_p \cdot e(t) + K_i \cdot \int_0^t e(t)dt + K_d \cdot \frac{de(t)}{dt} \tag{5.1}$$

5.1 Reference tracking

The objective of the controller is to follow some desired reference signal. In control systems technology this is known as reference tracking [22]. The reference in figure 5.2 is constructed based on thermal experiences that occur in real life. By doing so the results can give a first indication to what extend this thermal behaviour can be achieved.

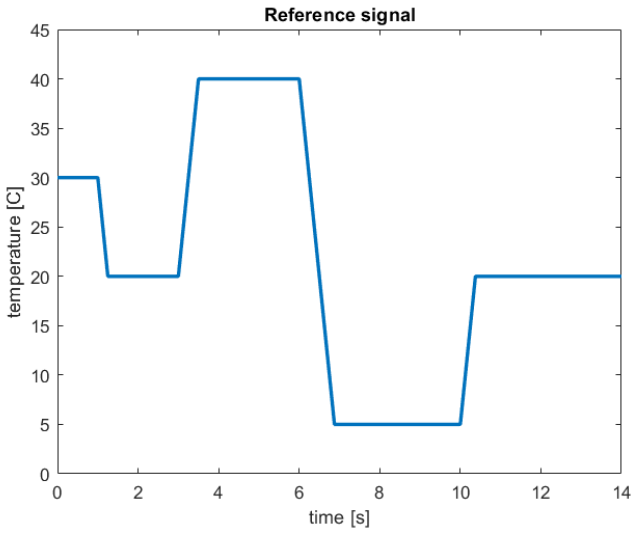

Figure 5.2: Reference signal for interface temperature

The reference in figure 5.2 incorporates both moderate and large temperature variations in both directions. Initially the temperature is set at 30 C, the following setpoint in the reference is 20 C which represents contact with a table that is room temperature, the next setpoint is 40 C and represents picking up a hot cup of coffee. The following setpoint is 5 C and represents picking up a cold glass of milk from the fridge, finially the reference reaches 20 C which represents the hands making contact with the table again. The reference is based on several extreme thermal sensations that can be expected to occur in real life, it is therefore important to simulate and evaluate the response of the haptic device on these conditions.

5.2 2D PID

The PID controller is first tested on a 2D Comsol model. This reduces computation time and provides fast iteration. Comsol has a built-in application that creates a PID controller which has the advantage that no extra software packages are needed that can significantly increase computation time and complicate the process. The disadvantage is that there are fewer possibilities to adjust and customise the controller. These built-in applications are easy to use but can be difficult to debug when unexpected behaviour is observed. The mathematical implementation of the controller is hardly visible to the user. In an attempt to create more understanding and have some way of validating the observed controller behaviour a separate Simulink model was made. This model incorporates a duplicate PID controller and a simplified model that is an approximation to the CFD model in Comsol. The following section explains how this simplified model is made.

5.2.1 System identification

Central in the simplified model is the plant model of the Comsol simulation. The plant model in the simplified model is a 2nd order transfer function according to equation 5.2. It has been previously shown in chapter 3.3 that the system behaves linearly. As a result it is possible to characterise the system with a step response. From this step response the coefficients in equation 5.2 can be determined [6].

$$T_f = \frac{g}{(\tau_1 s + 1)(\tau_2 s + 1)} \tag{5.2}$$

From a step response performed in Comsol two time constants and a steady state gain are deduced. This process is illustrated in figure 5.3, where in combination with the expressions in equation 5.3 three parameters are constructed, a gain g which indicates to what extent the response reaches the reference in steady state. The other parameters are Δt which is used to characterise the lag and t_{63}, the time at which 63% of the steady-state value is reached. These parameters are implemented in equation 5.2. Although the governing equation for heat transfer is first order 2.14 the transfer function used to represent the system is 2nd order [6]. This is done because the observed thermal behaviour at the contact interface exhibits a lag when exited with a step response. This lag is due to the time it takes the fluid to travel into the channel where the heat exchange can take place. This observed behaviour is best approximated with two time constants and thus a 2nd order transfer function.

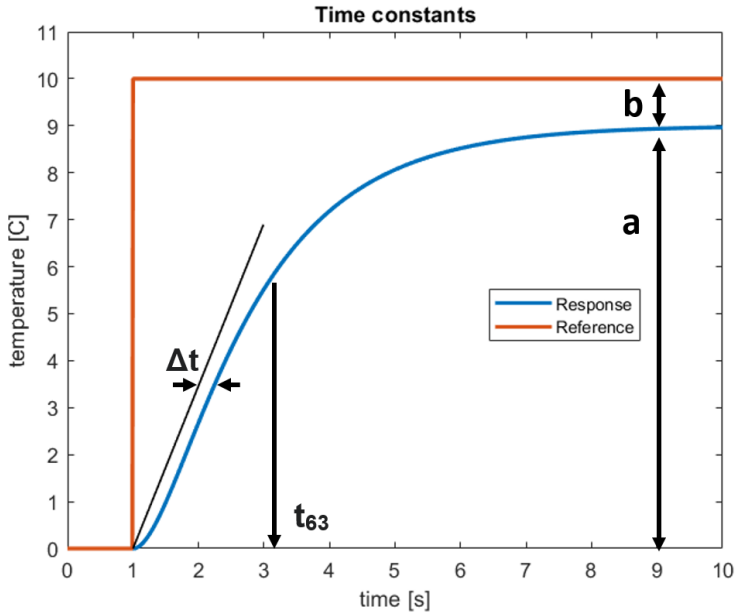

Figure 5.3: Determination of time constants Δt and t_{63} representing the lag and time 63% of the steady state response is reached. The steady state gain g is determined by a and b according to the ratio shown in equation 5.3

$$\tau_1 = \Delta t, \qquad \tau_2 = t_{63} - \Delta t, \qquad g = \frac{a}{a+b} \tag{5.3}$$

The transfer function in equation 5.2 should be a close approximation to the thermal behaviour of the interface. To check this, the transfer function is compared to 2D CFD model in Comsol in figure 5.4. It is for both models required to follow a reference that initially starts at 30 C and changes to 10 C at t=1 s. The inlet temperature is controlled to achieved the desired result. Both systems have identical PID controllers. The resulting responses are shown in figure 5.4, the blue and yellow lines represent the inlet temperature profiles for the Simulink model and Comsol model respectively. The achieved interface temperature is indicated by the red and purple lines for Simulink and Comsol respectively. It can be observed that the transfer function in Simulink quite accurately represents the thermal response of the CFD simulation in Comsol. This is especially interesting when realising that errors can propagate and accumulate in the separate PID loops, which can cause vastly different results.

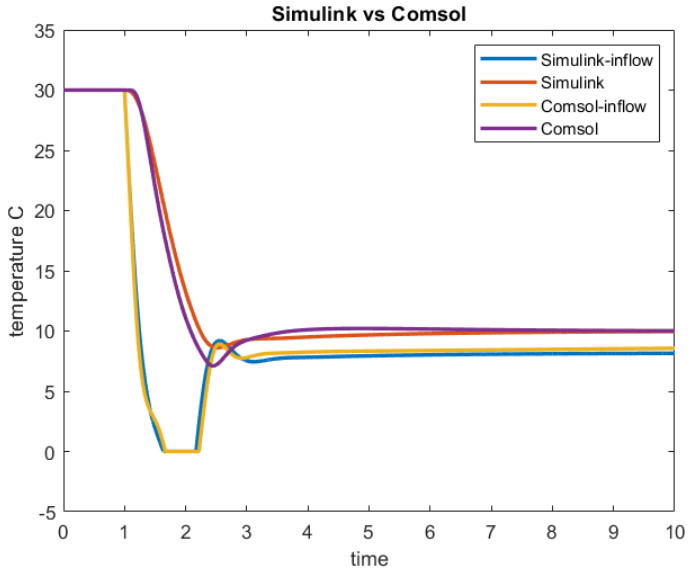

Figure 5.4: Comparison between identical PID controllers tested on Simulink model (based on transfer function 5.2) and 2D Comsol model, inflow temperatures for Simulink and Comsol in blue and yellow respectively, interface temperatures are shown with red and purple for Simulink and Comsol.

The Simulink model takes only seconds to solve and can therefore be applied to determine an approximate range in which optimal PID settings can be found. The Simulink model was also used to validate the observed behaviour in Comsol and in particular the process of debugging the embedded PID controller in Comsol.

5.3 2D PID Results

Figure 5.5 shows the results from a 2D Comsol simulation where PID control is applied. The 2D geometry has a channel diameter of 3 mm and a wall thickness of 1 mm.

The temperature reference is shown in red together with the inflow temperature in blue and resulting interface temperature response in yellow. The response shows a maximum overshoot of approximately 1 C, the steady state error is negligible. The gains for the PID controller are shown in table 5.1. Due to the slow nature of the system the integration action can grow fast, therefore the integrator gain K_i was set at 0.2. If larger integration action is desired there exists a method to circumvent this problem, which is known as anti-integral-windup. This prevents the accumulation of the integration action beyond a set limit.

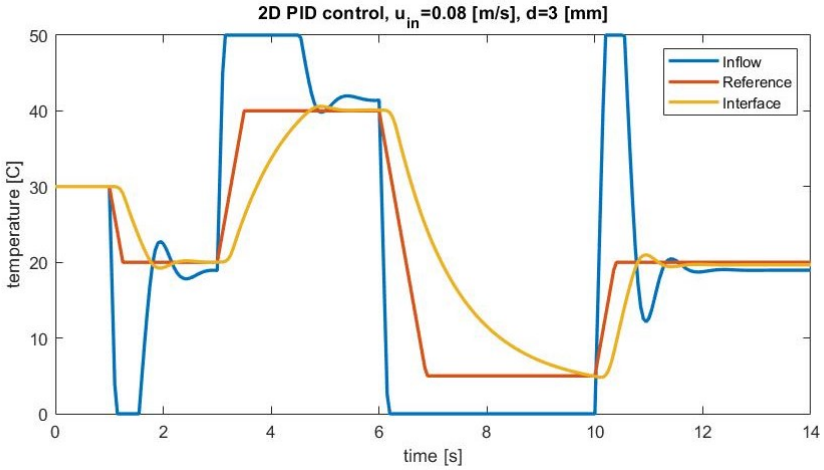

Figure 5.5: PID control of a 2D Comsol model

Table 5.1: 2D PID parameters

K_p	6
K_i	0.2
k_d	0.5

5.4 3D PID results

In 3D a similar PID controller is made, the 3D geometry being used is the simplified 3D model shown in figure 2.2b. The channel diameter is 3 mm and the wall thickness is 1 mm.

The resulting response is shown in figure 5.6. The red line indicates the desired temperature reference, the blue line represents the inflow temperature. The interface temperature is indicated by the yellow line. Both the overshoot and steady error have been practically been eliminated. The lag between the interface temperature and reference has been minimised, the reference cannot be reached faster as the inflow temperature is already constrained by its minimum and maximum values. The gains used in the 3D PID controller are a K_p value of 6, K_i value of 0.1 and a K_d value of 0.5.

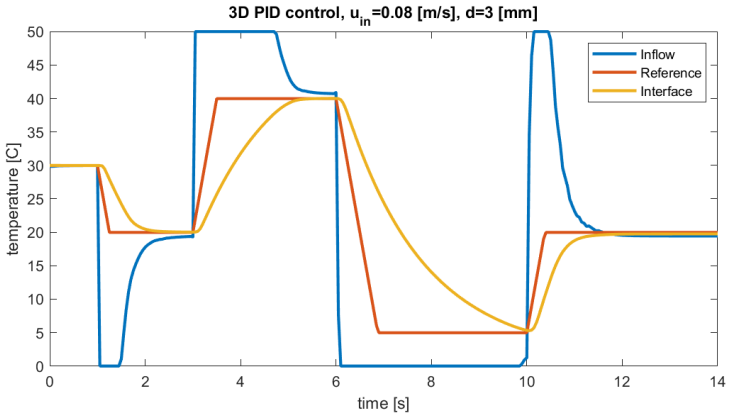

Figure 5.6: PID control of a 3D Comsol model

In order to give a more intuitive interpretation of the results shown in figure 5.6 the internal temperature field is visualised in figure 5.7. Four instances are chosen at which the temperature field is evaluated along a cross-section. The outline of the 3D geometry is left visible. At t=1.75 s, the first set point of 20 C is almost reached. At t=5 s the next set point of 40 C is almost reached. The following image at t=8 s shows the temperature field while cooling is applied to reach the set point of 5 C. At t=10.5 s the inlet temperature is almost 50 C, the internal gradients are largest here since the inlet temperature was changed from 0 C to 50 C at t=10 s. The internal temperature of the finger appears to remain constant. This is due to the low conductivity of the material in the finger and interface resistance. The scale used for the temperature ranges from 0 C to 50 C, it is therefore difficult to notice variations in the order of several degrees.

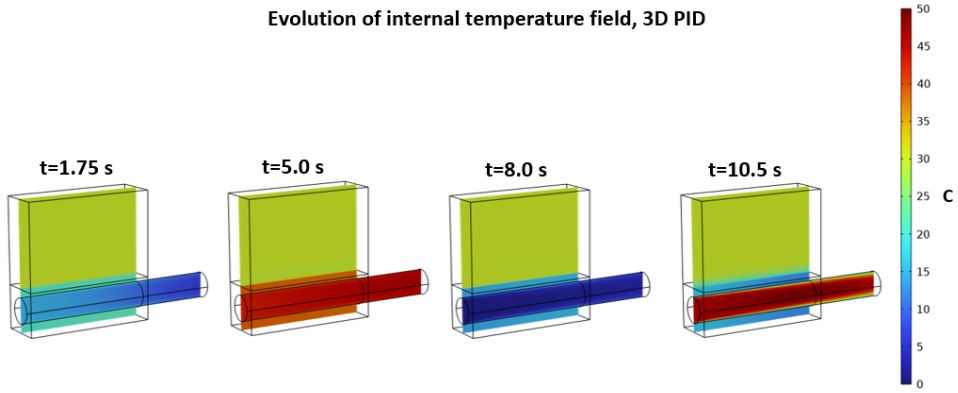

Figure 5.7: Evolution of the internal temperature field corresponding to the 3D PID simulation shown in figure 5.6

The response of the PID control in 2D and 3D contain a lot of similarity, which results from the fact that the 2D model is an approximation to the 3D model. The observation that the results are comparable indicates that the approximation is accurate and has retained the governing thermal characteristics. The gain parameters found with the 2D simulations listed in table 5.1 create a good starting point for the 3D simulations, the controller gains used for the controller in 3D are largely identical to 2D controller gains. It takes around 1 hour for the computer to solve the 3D simulation with PID controller shown in figure 5.6. The 2D simulations only take about 10 % of the time, it is therefore advised to do most of the tuning using 2D simulations.

The stability and robustness of the PID controllers were not investigated in detail. It is however important to at least test the effect of adding a disturbance to the system, as this can have detrimental effects on the controller performance. Both stability and robustness should therefore be considered if future research is conducted on the application of PID controllers on the thermal haptic device.

6 Model predictive control

Instead of using PID control it is possible to apply the knowledge gained about the system behaviour to design a more sophisticated control approach. With knowledge about the system behaviour it is possible to predict the response of future control actions. These predictions can be incorporated into the control strategy in a method known as model predictive control (MPC) [26]. Using this method an optimization procedure is solved providing the optimal short term control action. This optimisation procedure is performed in real time, as a consequence the computational hardware must be sufficiently fast to solve the set of equations within the set time step. A central element in achieving this short computation time is an efficient plant model with which the predictions can be performed.

A in-depth description of the MPC algorithm follows in the following section. First it is useful to examine the advantages of MPC and why it can be particularly useful in controlling interface temperature of the thermal haptic device, which has been listed below.

- MPC has the ability to take into account the future behaviour of the reference, this is known as preview capability [3].
- MPC can handle multiple input multiple output systems, where a change in each input affect more than one output. This can be particularly useful if both the inlet temperature and inlet velocity need to be controlled in future applications [3].
- In future research of the thermal haptic device it may very well be possible that nonlinear behaviour will play a significant role, for instance when turbulent flow conditions arise as a result of new system requirements. Another source of non-linearity could be large temperature differences that make the assumption of temperature independent material properties no longer valid. MPC has proven to be very effective in controlling non-linear system by making linear approximations of the systems behaviour. In some cases it is even possible to perform the full non-linear optimization procedure with advanced processors [14].

A central element in MPC is the plant model with which the future behaviour is predicted. The plant model in this application is a 2nd order transfer function which is constructed using the procedure elaborated previously in 5.2. Here a step response is used to construct a transfer function that models the behaviour of the interface temperature. This transfer function is relatively simple and can therefore be evaluated fast, this characteristic makes it especially suitable to serve as the plant model.

6.1 Method & Algorithm

In order to give a general understanding of the working principles of MPC figure 6.1 is examined. With the plant model represented by the 2nd order transfer function a number of future steps are predicted, the total number of future steps is referred to as the prediction horizon. Over the prediction horizon the control input is optimised. The optimization is performed by minimising an objective function. The optimization produces an optimal set of control actions for the full length of the prediction horizon, after which only the first control action is used. Next the prediction horizon shifts to the future by one time step and the process is repeated. It is important to note that this control process is inherently open-loop and is reinitialised by the feedback received at each time step.

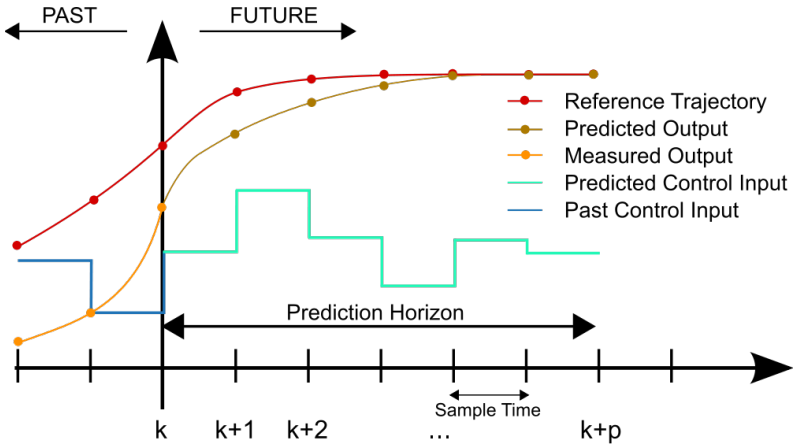

Figure 6.1: MPC algorithm

The objective function shown in equation 6.1 serves as cumulative measure of the future error in the predicted path as well as the amount of control effort needed [25]. The reference and interface temperature are represented by r_i and x_i respectively, the difference between r_i and x_i represents the error. The change in inlet temperature between two time steps is represented by Δu_i, both Δu_i and the error are squared to ensure both under and overshoot are penalised. As a consequence larger errors are penalised more than smaller errors. Both the error and Δu_i are evaluated over the prediction horizon N. The relative contribution of both factors can be adjusted with weighting factors w_{x_i} and w_{u_i}. In practise only the first few steps of the prediction horizon are kept variable in the optimization program as these have the most significant effect on the solution [25]. The section of the prediction horizon that is varied is called the control horizon and is often between 2 and 4 samples long. The size of the control horizon determines the computational complexity of the optimization problem and has a dominant influence on the computation time[3].

$$J = \sum_{i=1}^{N} w_x (r_i - x_i)^2 + \sum_{i=1}^{N} w_u \Delta u_i^2 \tag{6.1}$$

In practice equation 6.1 is rewritten into the matrix form shown in equation 6.2. Minimising this quadratic cost function can be done by a quadratic programming solver. The biggest strength of this approach is that instead of sampling the entire solution domain the derivatives will lead directly to the optimum of the convex cost function J. This procedure can be performed in the order of tens of milliseconds which make it practical for application in real systems.

$$J = \frac{1}{2}\mathbf{x}^T Q \mathbf{x} + C^T \mathbf{x} \tag{6.2}$$

MPC constraints

As mentioned earlier a major advantage of MPC is its ability to handle constraints. The constraints enter the optimization algorithm as inequality constrains. The constraints can be both hard and soft constraints. The soft constraints make it possible for the solver to find meaning full results when two constraints conflict with each other. Take the example where MPC is used for cruise control, when a car travels a steep hill it will be possible that the speed drops below the set constraint even with full throttle. If this constraint is set as a soft constraint, the algorithm will allow temporarily violating it. In practice constraints on the output are set as soft constraints, constraints on the input are set as hard constraints. In the system of the thermal haptic device the input is the inlet temperature and the output is the interface temperature.

6.2 Implementation

The complexity of the MPC algorithm makes it difficult and time consuming to implement in a fully self made computer code. However use can be made of the fact that the subject is not entirely new, Matlab Simulink has a built in MPC design application which supports this design process.

To evaluate the MPC performance it is tested on the CFD model in Comsol. It is required for Simulink to interact with the Comsol software where at each time step new control actions are fed into the Comsol model. The communication between Simulink and Comsol requires a Livelink software package which connects Simulink to Comsol. With the Livelink software a special block in Simulink is constructed which contains the Comsol model. Figure 6.2 provides an illustration of the setup in Simulink.

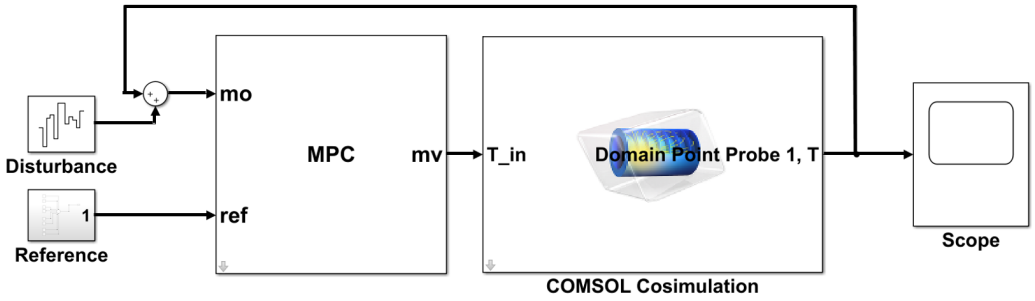

Figure 6.2: MPC layout in Simulink

The MPC block has two inputs, the reference signal and the output of the Comsol model, which includes a random disturbance. The Comsol model has one input and one output, inflow temperature and interface temperature respectively. As mentioned earlier it is possible to extend the number of ins and outputs. Internally the MPC block executes the optimization program and communicates with the Comsol model every 0.1 second. It is important to note that a transient Comsol simulation of 10 seconds will take tens of minutes to solve. If the MPC is configured to update the control action every 0.1 second the optimization procedure in the controller will have much time to solve as this time step of 0.1 seconds will take Comsol several seconds to solve. If the controller needs more than 0.1 second to solve, the simulation will still run fine since the plant model represented by the CFD model in Comsol forms a bottle-neck. However no doubt should exist about the controller‘s ability to solve fast enough, recent attempts using analog circuitry have solved quadratic programming problems in the order micro seconds [29].

6.3 MPC Parameters

The parameters that are used for both MPC controllers are listed in table 6.1. There exist hand rules which facilitate in determining these parameters. Considering the prediction horizon it is advised to place at least 10 samples in the typical rise time of the system. The length of the prediction horizon should be long enough to capture the relevant dynamics. A horizon of 20 samples was chosen which satisfies the mentioned hand rules. The typical size of a control horizon lies between 2 and 4, a larger size will greatly increase the complexity of the optimization program and therefore the computational load. Here a control horizon of 3 was chosen. The weights in the objective function can be particularly useful in the case of system containing multiple in and outputs. However in this case there is one input, the inlet temperature, and one output, the interface temperature. At the start of the research it was concluded that in this research the inlet temperature could change instantly. Therefore the weights w_x and w_u could be set at 1 and 0 respectively, however this will create errors and unstable behaviour which is why this value for w_u was changed to 0.1.

Table 6.1: MPC parameters

Time step	0.1 [s]
Prediction horizon	20
Control horizon	3
w_x	1
w_u	0.1

6.4 Results & Comparison with PID

Figure 6.3 shows the results from a 2D simulation where MPC is used to control the interface temperature by changing the inlet temperature. Essentially the principle of reference tracking used in chapter 5.3 is applied again, the difference being that instead of a PID controller MPC is used.

It can be observed that the interface temperature reaches the desired reference. The overshoot is small and the steady state error is negligible. The inflow temperature reaches the constrained limits, the resulting rise time between the reference and the interface temperature can therefore not be decreased further. A disturbance is added to the measured signal in order to review the stability of the control system, the maximum amplitude of this random signal is 2 C. This signal is a first estimate of a large disturbance and gives a idea about of the stability of the controller. In figure 6.3 it can be seen that the resulting response is stable in the presence of this disturbance.

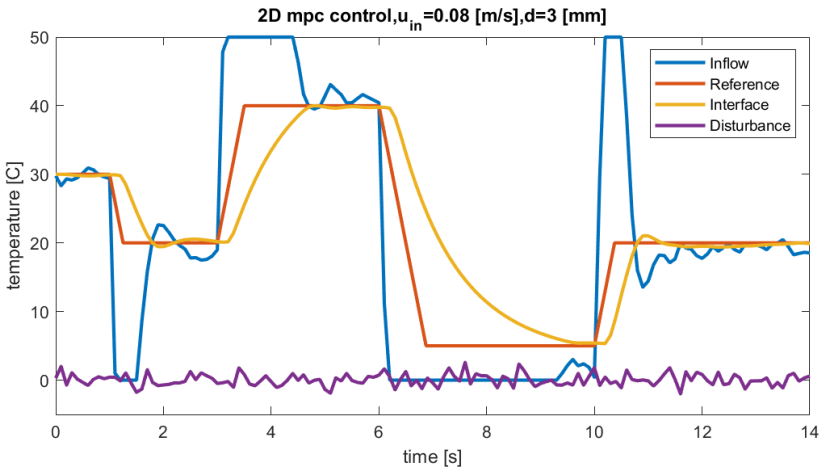

Figure 6.3: MPC control of a 2D system, including disturbance

A MPC controller was tested on a 3D setup as well. The geometry being used is a copy of the geometry used in figure 5.6.

Figure 6.4 shows the results of a 3D MPC simulation performed on the geometry shown in 2.2b. The interface temperature exhibits a slight overshoot which is less than 0.5 C, the steady state error is negligible. The added disturbance did not create unstable behaviour, it is possible that a noise signal with higher frequency content or larger magnitude will have other effects, but these have not been investigated in this research. For now it is observed that the response of the system appears stable in the presence of a significant disturbance.

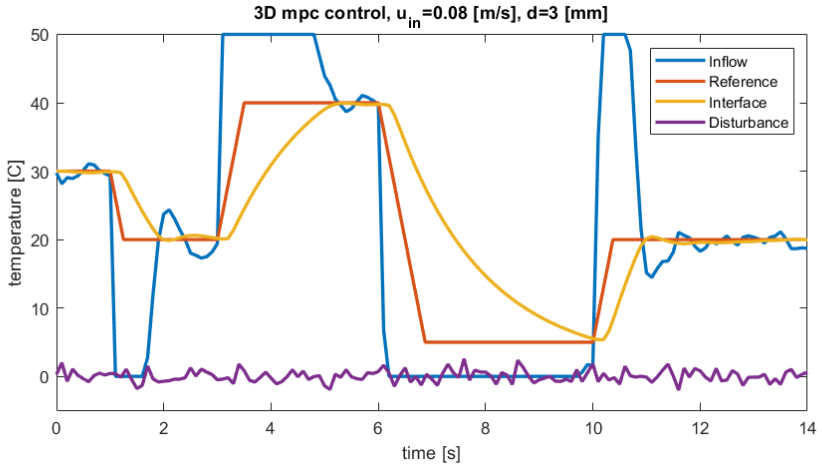

Figure 6.4: MPC control of a 3D system, including disturbance

Figure 6.5 shows the internal temperature field along a cross-section for the 3D MPC simulation shown in figure 6.4. These temperature fields are almost indistinguishable from the internal temperature fields shown in figure 5.7. This is in line with the observed performance of the PID and MPC controller, which have shown similar performance in both the observed overshoot and steady-state error as well as the overall trajectory of the interface temperature. From the apparent similarities in the observed results no clear preference for either PID or MPC can be constructed. It is however likely that in the future conditions arise where MPC will outperform PID according to the advantages of MPC mentioned at the beginning of this chapter. The preliminary study performed into both PID control and MPC have indicated that both methods can be used to control the thermal haptic device. However more research is needed in order make stronger conclusions on the performance of both methods.

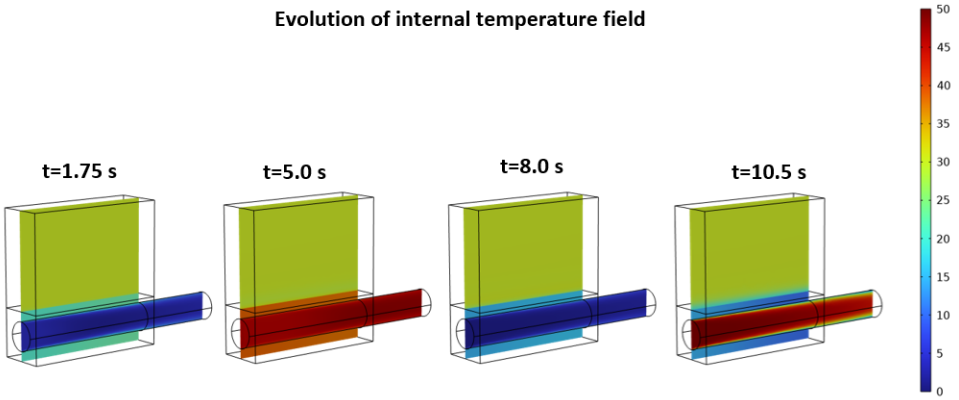

Figure 6.5: Evolution of the internal temperature field corresponding to the 3D MPC simulation shown in figure 6.4

7 Preliminary geometry optimization

In this chapter a start is made with the geometric optimization of the 3D design. In chapter 4 a start was made with analysis of a simplified 3D geometry shown in figure 4.1, in this chapter the analysis is extended to designs containing multiple channels.

The characterisation of the thermal behaviour in chapter 3 showed that the transfer between inlet and interface temperature increases when the wall thickness and channel diameter are decreased. Further dimensionless analysis into the response time of a 3D geometry performed in chapter 4 has again showed the dominant effect of reducing the wall thickness. It was observed that a decrease in dimensionless wall thickness yields a faster dimensionless response time. Extending this analysis to a design containing multiple channels the following constraints have to be taken into consideration. The minimum wall thickness has previously been set at 1 mm. Dimensions of the contact interface are 15 x 15 mm. When these constrains are honored the only remaining variable is the number of channels. Three possible designs are shown in figure 7.1 on which the preliminary optimization will be focused.

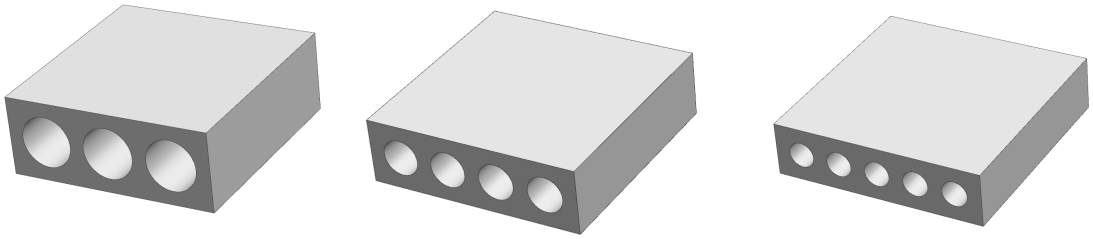

(a) Diameter = 11/3 [mm] (b) Diameter = 10/4 [mm] (c) Diameter = 9/5 [mm]

Figure 7.1: 3D design concepts

The designs shown in figure 7.1 have a minimal solid volume for a given number of channels. A minimum volume will reduce the amount of heat transferred to heat up or cool down the device, which will increase the overall efficiency of the system and can have a positive effect on the response time . Figure 7.2 is used to illustrate this effect. The total amount of heat transfer to the liquid is represented by the blue line, the red line shows the heat transfer over the contact interface. This is an arbitrary step response simulation including the 3D geometry shown in 4.1. The heat transfer over the contact interface represent only a small fraction of the total heat transfer. The area between the lines represents the amount of heat transfer used to change the temperature of the device. This area can be represented by equation 7.1 with Q_d, the solid volume of the device is represented by V, ρ_a and Cp_a represent the density and thermal capacity of aluminium, the increase in temperature is denoted with T. Equation 7.1 shows the only way to decrease Q_d using the geometry, is to reduce the solid volume V.

$$Q_d = V \cdot \rho_a \cdot Cp_a \cdot \Delta T \tag{7.1}$$

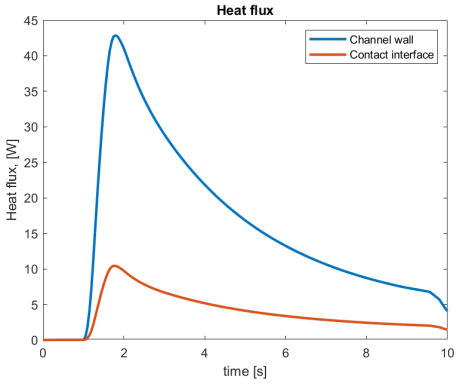

Figure 7.2: Comparison between the total heat flux and flux originating from the finger

In performing an optimization it must first be clear what is considered to be optimal. In evaluating the different designs shown in figure 7.1 the fasted response time of the interface temperature is used to determine the optimal design. Simulations consist of a step response where the mass flow is kept constant for all designs. Initially the system is at 30 C, at t=1 s the inflow temperature is changed to 0 C.

7.1 Results

The solid volume of the 3 designs is shown in table 7.1. The design with 5 channels has the lowest solid volume and can therefore be expected to achieve the fastest response, considering all geometries are subjected to the same mass flux. Figure 7.3a shows the interface temperature as a function of time for the 3 designs. It can be observed that instead of the design with small channels and minimal volume, the intermediate design with 4 channels performs best by achieving the fastest thermal response. This is especially interesting considering the mass flow is constant for all 3 designs, which means that the inlet velocity is highest for the design with 5 channels.

A possible explanation for this effect is, by reducing the channel diameter the fluid-solid contact surface is reduced as well. The effect of a reduction in surface area will need to be compensated by an increase in heat transfer due the higher flow velocity. The combination of both effect can cause the design with 4 channels to outperform the other designs, based on the response time of the interface temperature.

Similar behaviour can be seen in figure 7.3b, where the heat flux through the channel wall is shown. The design with 4 channels is able to transport the largest heat flux to the fluid even though it does not have the highest average flow velocity. This is especially interesting as it suggest the presence of an unconstrained optimum. Something that was not observed in the 2D and asymmetric simulations and appears to be a 3D phenomenon. These observations give a first indication where an optimal design can be found. It is possible that in other conditions a different design performs optimal. This is therefore a subject where further research is needed to create stronger conclusions.

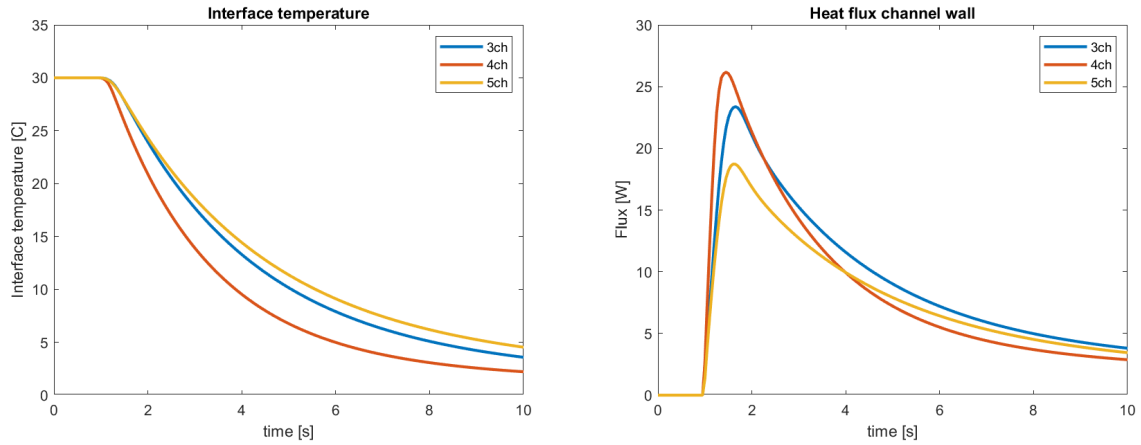

(a) Interface temperature

(b) Total heat flux across channel wall

Figure 7.3: Resulting interface temperature profile and heat flux from step response simulation

Table 7.1: Volume

	Solid volume $[mm^3]$	Channel diameter [mm]
Design 3 channels	800	11/3
Design 4 channels	718	10/4
Design 5 channels	664	9/5

8 Discussion & Recommendations

During this research it is not possible to cover every subject in full detail. Along the way assumptions are made to ensure progress can be made. In future research it is possible to extend the knowledge by reconsidering these assumptions. In this chapter several subjects are mentioned that were not considered in this research but can nevertheless be interesting subjects for future research.

At the start of the research is was assumed that no constrain is placed on the rate with which the inlet temperature can change. In real life hardware will put some constraints on this rate, it is therefore interesting to see if the inlet temperature profiles used in this research can be achieved in real life.

The 3D geometries all had channels with a circular cross-section. In chapter 7 it has been shown that minimising the solid volume of the device reduces the thermal inertia and can increase the performance. It is therefore interesting to see what the effect of using non-circular ducts is on the performance. By using square channels the solid volume can be reduced and the heat transferring area between solid and liquid can be increased. Both effects can have a positive effect on the performance.

The effect of manifolds, valves and other hardware such as suitable pumps have not been investigated. These additional components can have a significant impact on the performance. It can be useful to investigate these components to gain a better understanding of the possibilities and constraints of the total system.

Central in this research was the notion that only laminar flow regimes would be investigated. It can, for optimisation purposes, be useful to incorporate higher flow speeds to reach faster response times. It is possible that under these more extreme conditions turbulence is able to occur. Another interesting notion is that turbulence induces mixing and can therefore have a positive effect on heat transfer. This effect can be strong and play a significant role in achieving optimal performance, which is why it can be interesting to include turbulent flow conditions in the future design process.

The dimensionless analysis in chapter 4 has yielded a basic characterisation of the system. It can be useful to extend this analysis which can yield a deeper understanding of the thermal response of the system. One particular aspect that should receive extra attention in further research is the interface resistance. In the final analysis of the dimensionless study it was observed that the dimensionless interface resistance was not kept constant in all simulations. Which means that some of the observed behaviour in chapter 4 could be the consequence of an incorrect application of the dimensionless interface resistance.

9 Conclusion

The preliminary research objective at the very beginning was to find some way to emulate thermal behaviour. The low efficiency and large heat generation were the primary reason why Peltier elements where discarded as a viable option in the introductory chapter. Instead of using a water cooled Peltier elements this research focused on using the water directly to emulate thermal behaviour.

In order to characterise the thermal behaviour a range of simulations where performed. Beginning with 2D simulations that focused on the relation between the inlet temperature and interface temperature. For sinusoidal inlet temperature profiles it was investigated how this profile transfers to the contact interface. Sine waves with higher frequencies reached the interface with lower amplitude, this relation between frequency and observed amplitude followed a logarithmic profile. Smaller channels, thinner walls and increased velocity independently showed to increase the transfer between the inlet temperature and interface temperature. This conclusion was further strengthened by the observation that increasing the inlet velocity and decreasing the size of channels and walls will result in a faster step response. The optimum for the fastest response time is a constrained optimum, indicating that the constraints for minimum channel size, wall thickness and maximum inlet velocity are deciding factors in the transient behaviour of the system. The following axi-symmetric simulations showed similar results as previously observed in 2D. In order to make more general conclusions about the systems behaviour a dimensionless analysis was performed on a 3D approximation of the full system. A series of simulations are performed where the dimensionless wall thickness and Peclet number of the flow are changed. The resulting response time of the interface temperature and maximum heat flux magnitude in the channel wall where evaluated. The fastest dimensionless response time was observed for the smallest dimensionless wall thickness and the highest Peclet number. A change in dimensionless wall thickness has a dominant effect on the response time. The dimensionless heat flux represented by ϵ, also known as the effectiveness, was evaluated for the same range of simulations. The results give a basic characterisation of the thermal behaviour of the system. The interpretation of the results has only been preliminary discussed. A more in-depth discussion can be performed in future research.

In order to get a preliminary understanding regarding the control of the interface temperature. Both PID and MPC control are tested on a 2D and 3D geometry. The objective for the interface temperature is to follow a reference trajectory by means of reference tracking. This reference represents several thermal sensations that can occur in daily life. PID control showed good control with minimal overshoot and negligible steady-state error. It was however not reviewed how robust this control strategy is in the presence of a noise signal. In the future it is likely that PID control will not be sufficient. Therefore the more advanced control method, Model Predictive Control was applied. The resulting temperature response followed the desired reference and remained stable in the presence of a disturbance for both the 2D and the 3D case. There was minimal overshoot and negligible steady state error. From the results it was concluded that MPC control can successfully be implemented and provides a viable option for the control of a future thermal haptic device. The research into both control methods have yielded valuable results, however more research is needed before strong conclusions can be drawn.

Most of the analysis has focused on 2D and an approximation of the 3D problem. The optimization of the full 3D design has only preliminary been discussed in chapter 7. Nevertheless interesting observations are made, most notably the presence of a unconstrained optimum indicating that a design with 4 channels achieves optimal performance. There is additional research needed to convert these observations into strong conclusions, which could be an interesting topic for follow up research.

To conclude, in this thesis a overview has been created of the possibilities of using a liquid based thermal haptic device. Including a characterisation of the relevant thermal dynamics as well as a preliminary study into the application of PID and MPC control, which has shown the viability of both methods. As start has been made to perform an optimization on the full 3D geometry which has indicated that the optimum could be a design with 4 channels.

References

[1] RS Components B.V. *Peltier element 19x19mm*. https://nl.rs-online.com/web/p/peltier-modules/1743116. (accessed September 30, 2021).

[2] bol.com. *VR heatset*. https://www.bol.com/nl/nl/p/oculus-quest-64-gb-vr-brille-3d-virtual-reality-headset/9200000116515878/?bltgh=q0mFSXnAmezPGwDpGp5JXQ.2_34.37.ProductTitle. (accessed September 30, 2021).

[3] Eduardo F Camacho and Carlos Bordons Alba. *Model predictive control*. Springer science & business media, 2003.

[4] Fang Chen, Håkan Nilsson, and Ingvar Holmér. "Evaluation of hand and finger heat loss with a heated hand model". In: *Journal of Physiological Anthropology and Applied Human Science* 18.4 (1999), pp. 135–140. ISSN: 13453475. DOI: 10.2114/jpa.18.135.

[5] DDPrototype. *DESIGN FOR CNC MACHINING*. https://www.ddprototype.com/design-for-cnc-machining/. (accessed April 2nd, 2022).

[6] Dr John Ebert. *Modeling feedback control of thermal systems*. https://www.comsol.com/video/simulating-feedback-control-thermal-systems. (accessed March 30th , 2022).

[7] Eli Eliav and Richard H. Gracely. "Measuring and assessing pain". In: *Orofacial Pain and Headache* (2008), pp. 45–56. DOI: 10.1016/B978-0-7234-3412-2.10003-3.

[8] "Emerging Thermal Technology Enabled Augmented Reality". In: *Advanced Functional Materials* 2007952.June (2021). ISSN: 16163028. DOI: 10.1002/adfm.202007952.

[9] Massimiliano Gabardi et al. "Development of a miniaturized thermal module designed for integration in a wearable haptic device". In: *IEEE Haptics Symposium, HAPTICS* 2018-March (2018), pp. 100–105. ISSN: 23247355. DOI: 10.1109/HAPTICS.2018.8357160.

[10] Simon Gallo et al. "Towards multimodal haptics for teleoperation: Design of a tactile thermal display". In: *International Workshop on Advanced Motion Control, AMC* (2012), pp. 1–5. DOI: 10.1109/AMC.2012.6197145.

[11] H. Julian Goldsmid. "Bismuth telluride and its alloys as materials for thermoelectric generation". In: *Materials* 7.4 (2014), pp. 2577–2592. ISSN: 19961944. DOI: 10.3390/ma7042577.

[12] Mohamed Guiatni and Abderrahmane Kheddar. "Theoretical and experimental study of a heat transfer model for thermal feedback in virtual environments". In: *2008 IEEE/RSJ International Conference on Intelligent Robots and Systems, IROS* (2008), pp. 2996–3001. DOI: 10.1109/IROS.2008.4650687.

[13] Hsin-ni Ho and Lynette A Jones. "Contribution of thermal cues to material discrimination and localization". In: 68.1 (2006), pp. 118–128.

[14] Reza Kamyar and Ehsan Taheri. "Aircraft Optimal Terrain/Threat-Based Trajectory Planning and Control". In: *Journal of Guidance, Control, and Dynamics* 34 (2014), pp. 466–483. ISSN: 00981354. DOI: 10.1016/j.jprocont.2011.10.008.

[15] Mingyu Kim, Changyu Jeon, and Jinmo Kim. "A Study on Immersion and Presence of a Portable Hand Haptic System for Immersive Virtual Reality". In: *Sensors (Basel, Switzerland)* 17.5 (2017). ISSN: 14248220. DOI: 10.3390/s17051141.

[16] Sven Kratz and Tony Dunnigan. "ThermoTouch: Design of a high dynamic temperature range thermal haptic display". In: *Conference on Human Factors in Computing Systems - Proceedings* 07-12-May-2016 (2016), pp. 1577–1582. DOI: 10.1145/2851581.2892554.

[17] Jinwoo Lee et al. "Stretchable Skin-Like Cooling/Heating Device for Reconstruction of Artificial Thermal Sensation in Virtual Reality". In: *Advanced Functional Materials* 30.29 (2020), pp. 1–11. ISSN: 16163028. DOI: 10.1002/adfm.201909171.

[18] Jinwoo Lee et al. “Thermo-Haptic Materials and Devices for Wearable Virtual and Augmented Reality”. In: *Advanced Functional Materials* 2007376 (2020). ISSN: 16163028. DOI: 10.1002/adfm.202007376.

[19] Lijuan Liu et al. *FlowGlove: A Liquid-Based Wearable Device for Haptic Interaction in Virtual Reality*. Vol. 12429 LNCS. Springer International Publishing, 2020, pp. 316–331. ISBN: 9783030599867. DOI: 10.1007/978-3-030-59987-4_23. URL: http://dx.doi.org/10.1007/978-3-030-59987-4%7B%5C_%7D23.

[20] Takaki Murakami et al. “Altered touch: Miniature haptic display with force, thermal and tactile feedback for augmented haptics”. In: *ACM SIGGRAPH 2017 Posters, SIGGRAPH 2017* (2017). DOI: 10.1145/3102163.3102225.

[21] Frans TM Nieuwstadt, Jerry Westerweel, and Bendiks J Boersma. *Turbulence: introduction to theory and applications of turbulent flows*. Springer, 2016.

[22] Julio E. Normey-Rico et al. “Mobile robot path tracking using a robust PID controller”. In: *Control Engineering Practice* 9.11 (2001), pp. 1209–1214. ISSN: 09670661. DOI: 10.1016/S0967-0661(01)00066-1.

[23] Jinhyeok Oh et al. “A Liquid Metal Based Multimodal Sensor and Haptic Feedback Device for Thermal and Tactile Sensation Generation in Virtual Reality”. In: *Advanced Functional Materials* 2007772 (2020), pp. 1–10. ISSN: 16163028. DOI: 10.1002/adfm.202007772.

[24] Jerome Perret and Emmanuel Vander Poorten. “Review Paper : Commercial Haptic Gloves”. In: *The Industrial Track of EuroVR 2018 : Proceedings of the 15th Annual EuroVR Conference* (2018), pp. 39–46. ISSN: 2242-122X. URL: https://ieeexplore.ieee.org/abstract/document/8470813/%7B%5C%%7D0Ahttps://cris.vtt.fi/en/publications/the-industrial-track-of-eurovr-2018-proceedings-of-the-15th-annua.

[25] S. Joe Qin and Thomas A. Badgwell. “A survey of industrial model predictive control technology”. In: *Control Engineering Practice* 11.7 (2003), pp. 733–764. ISSN: 09670661. DOI: 10.1016/S0967-0661(02)00186-7.

[26] James B. Rawlings. “Tutorial overview of Model Predictive Control”. In: *IEEE Control Systems Magazine* 20.3 (2000), pp. 22–24. ISSN: 02721708.

[27] Konrad Rykaczewski. “Modeling thermal contact resistance at the finger-object interface”. In: *Temperature* 6.1 (2019), pp. 85–95. ISSN: 23328959. DOI: 10.1080/23328940.2018.1551706. URL: https://doi.org/10.1080/23328940.2018.1551706.

[28] “Spatial acuity and summation on the hand: The role of thermal cues in material discrimination”. In: 71.7 (2009), pp. 1439–1459. DOI: 10.3758/APP.

[29] Sergey Vichik and Francesco Borrelli. “Solving linear and quadratic programs with an analog circuit”. In: *Computers and Chemical Engineering* 70 (2014), pp. 160–171. ISSN: 00981354. DOI: 10.1016/j.compchemeng.2014.01.011.

[30] Steven D. Waldman. “CHAPTER 109 - Functional Anatomy of the Thermoreceptors”. In: *Pain Review*. Ed. by Steven D. Waldman. Philadelphia: W.B. Saunders, 2009, p. 190. ISBN: 978-1-4160-5893-9. DOI: https://doi.org/10.1016/B978-1-4160-5893-9.00109-X. URL: https://www.sciencedirect.com/science/article/pii/B978141605893900109X.

[31] Tae Heon Yang et al. “Recent Advances and Opportunities of Active Materials for Haptic Technologies in Virtual and Augmented Reality”. In: *Advanced Functional Materials* 2008831.March (2021). ISSN: 16163028. DOI: 10.1002/adfm.202008831.